Journal of Medicinal Chemistry

pubs.acs.org/jmc

Article

An Enhanced Cancer Immunogenic Cell Death Strategy: Fibrate-Oxaliplatin(IV) Conjugates with Modulating Tumor Immune Microenvironment

Xue-Jiao Liang,[1] Xu Guo,[1] Peng-Hui Zhu, Zi-Han Zhao, Zhihao You, Kan Yang, Yali Song, Longfei Li,* and Xue-Qing Song*

Cite This: *J. Med. Chem.* 2025, 68, 26328−26347

Read Online

ACCESS | Metrics & More | Article Recommendations | Supporting Information

ABSTRACT: The present immunogenic cell death (ICD) strategies remain far from being suitable for effective clinical applications, highlighting the urgent need for novel strategies. Herein, the oxaliplatin-like fibrate-derived platinum(IV) conjugates **2**−**7** were designed and synthesized to explore novel approaches for enhancing ICD via modulation of tumor microenvironment (TME). Bioactivity evaluations showed that these conjugates accumulated highly in cells and released active components, exerting cytotoxicity. Especially, **5** exhibited 319-fold higher cytotoxicity than oxaliplatin. Mechanistic studies revealed that these conjugates induced severe DNA damage, mitochondrial dysfunction, and endoplasmic reticulum stress, ultimately activating the apoptotic pathway. Importantly, these events interacted with cholesterol metabolic regulation to form a self-amplifying cycle, which substantially enhanced damage-associated molecular pattern release to strengthen ICD and further modulated the TME by promoting $CD8^+$ T cell infiltration and cytokine secretion while downregulating PD-L1 expression and Treg-mediated immunosuppression. *In vivo*, these conjugates exhibited favorable biocompatibility, potent antitumor activity and reduced toxicity compared to oxaliplatin.

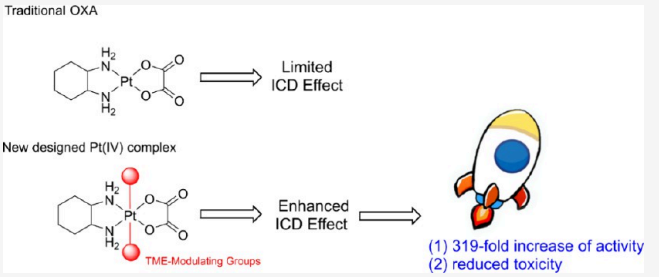

1. INTRODUCTION

One major challenge in current cancer therapies is immune escape, a phenomenon in which tumor cells evade recognition and attack by the immune system, thereby promoting tumor cell survival and potential progression.[1] Immunogenic cell death (ICD) is a unique form of programmed cell death that can stimulate the release of damage-associated molecular patterns (DAMPs) from dying tumor cells, including surface-exposed calreticulin (CRT), high-mobility group box 1 protein (HMGB1), and adenosine triphosphate (ATP).[2] These DAMPs effectively activate dendritic cells (DCs) and initiate antitumor T cell, thereby counteracting immune escape.[3,4] Given the crucial role of ICD in cancer immunotherapy, various induction strategies have been developed, such as chemotherapy, physical therapy, and biologics.[5] Among them, chemotherapy remains a cornerstone of comprehensive cancer treatment. Over the past few years, numerous chemotherapeutic agents including but not limited to metal complexes, anthracyclines, actinomycin D, lurbinectedin, and paclitaxel, demonstrated to effectively induce ICD.[6−8] Nevertheless, these reported chemotherapeutic agents remain far from being suitable for effective clinical application (restricted by the immunosuppressive microenvironment, high-dose toxicity, etc.), highlighting the urgent need for the development of novel ICD strategies.

Tumor metabolic reprogramming, particularly in cholesterol metabolism, not only promotes tumor proliferation and metastasis but also exerts a significant influence on tumor immune microenvironment.[9−11] Abnormal accumulation of cholesterol has been shown to impair antigen presentation, facilitate the infiltration of immunosuppressive cells, and directly inhibit the release of DAMPs, ultimately contributing to immune evasion.[12,13] Notably, endoplasmic reticulum stress (ERS) functions as a central cellular hub for stress sensing and signaling critical cellular stress sensing and signaling hub, and sustained activation of ERS has been identified as a key upstream event in the induction of ICD.[14−16] ERS activates the unfolded protein response (UPR) pathway, leading to increased production of reactive oxygen species (ROS), disruption of calcium homeostasis, and ultimately inducing the release of key DAMPs, such as CRT translocation.[17−19] Studies have demonstrated that cholesterol, as a major

Received: August 26, 2025
Revised: October 23, 2025
Accepted: November 27, 2025
Published: December 9, 2025

https://doi.org/10.1021/acs.jmedchem.5c02436
J. Med. Chem. 2025, 68, 26328−26347

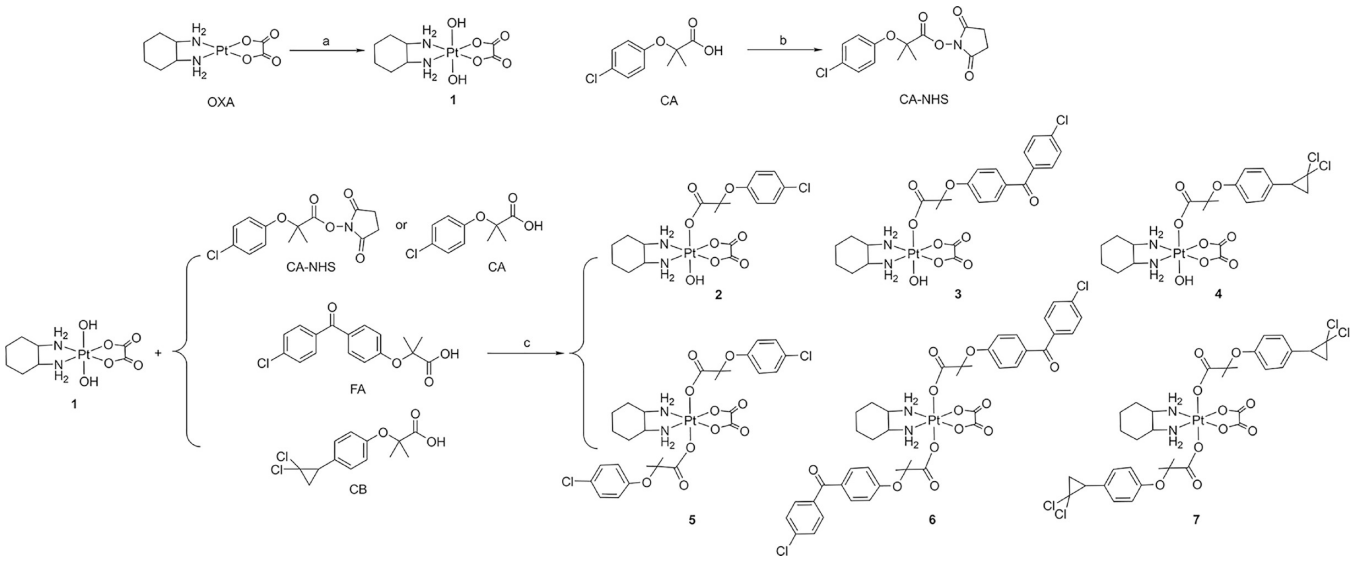

Figure 1. Synthetic routes of compounds **1**−**7**. Reagents and conditions: (a) H_2O_2, 70 °C, 7 h; (b) DCC, NHS, 25 °C, 24 h. (c) 2: CA-NHS, DMSO, 40 °C, 72 h; 3: FA, DMSO, TBTU, TEA, 40 °C, 24 h; 4: CB, DMSO, TBTU, TEA, 40 °C, 48 h; 5−7: CA/FA/CB, DMF, TBTU, TEA, 40 °C, 48 h.

Scheme 1. Schematic Diagram of the Mechanism by which Fibrate-Oxaliplatin(IV) Conjugate Regulates Cholesterol Metabolism to Exert Chemotherapy-Immune Synergistic Therapy.[a]

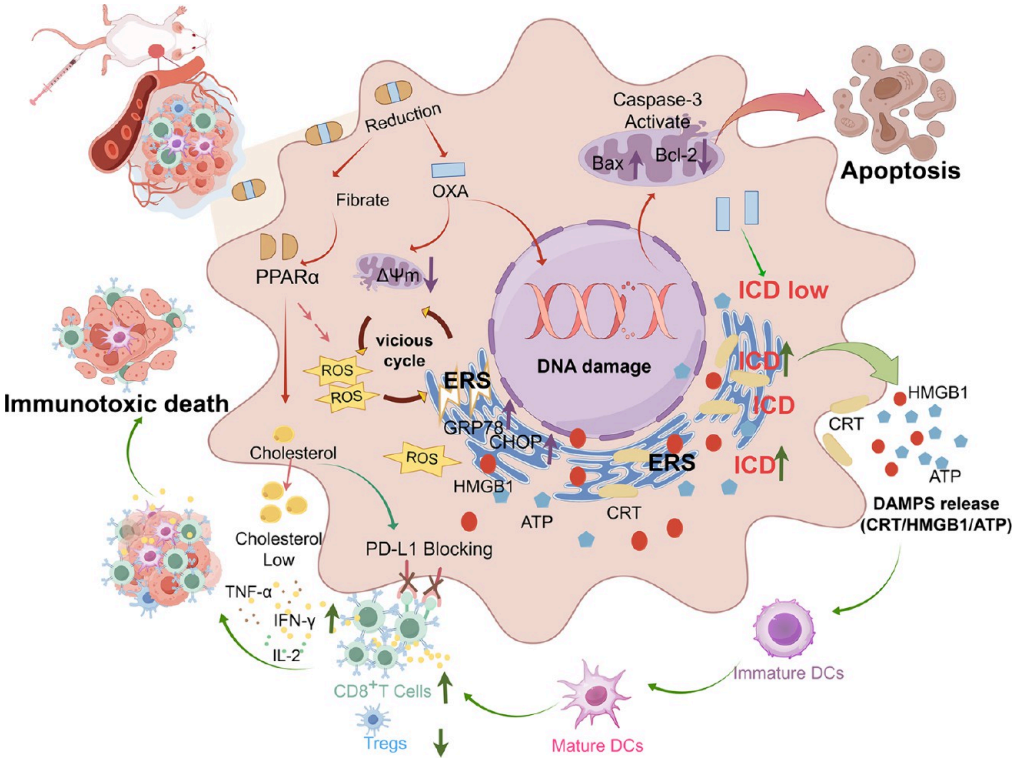

[a]Abbreviation: Bax, Bcl-2 Associated X; Bcl-2, B-Cell Lymphoma 2; CHOP, C/EBP-homologous protein; GRP78, glucose-regulated protein 78; IFN-γ, interferon-γ; tumor necrosis factor-α, TNF-α; interleukin-2, IL-2.

component of the endoplasmic reticulum membrane, plays a pivotal role in maintaining the lipid microenvironment. Its depletion disrupts this balance and triggers UPR activation.[20] Furthermore, structural and functional disruption of the endoplasmic reticulum can impact lipid metabolism.[21] Severe ERS has been shown to induce ICD and promote protective antitumor immunity.[22] From this perspective, effective regulation of cholesterol metabolism may be a viable strategy to reverse the "immune cold" phenotype of tumor cells and enhance their immunogenic performance.

Fibrate drugs (e.g., fenofibrate, clofibrate, and ciprofibrate) are widely used lipid-lowering agents in clinical practice, mainly targeting peroxisome proliferator-activated receptor α (PPARα) to regulate the expression of genes involved in lipid metabolism.[23−25] Remarkably, in addition to their well-established role in lipid regulation, accumulating evidence

https://doi.org/10.1021/acs.jmedchem.5c02436
J. Med. Chem. 2025, 68, 26328−26347

Table 1. IC_{50} Values (μM) of the Investigated Compounds against Cancer Cell Lines (4T1, MCF-7, A2780) and the Normal Cell Lines (HK2 and HUVEC) Evaluated by the MTT Assay[a]

	MCF-7		A2780		4T1		HUVEC	HK2		
Cell	24 h	72 h	24 h	72 h	24 h	72 h	72 h	72 h	SI[b]	SI[c]
CA	31.6 ± 0.9	26.0 ± 2.6	>100	52.3 ± 1.5	51.6 ± 2.8	25.2 ± 1.0	60.4 ± 1.1	34.9 ± 3.9	2.3	1.3
FA	32.3 ± 0.9	25.1 ± 2.7	>100	51.6 ± 5.5	28.2 ± 7.4	19.0 ± 2.3	42.6 ± 2.2	35.1 ± 1.4	1.7	1.4
CB	34.1 ± 2.9	18.5 ± 0.2	>100	48.1 ± 8.2	46.5 ± 1.5	26.2 ± 3.5	60.6 ± 4.2	36.9 ± 3.7	3.3	2.0
OXA	51.9 ± 13.2	25.5 ± 0.5	70.9 ± 5.4	4.6 ± 0.3	43.2 ± 25.9	15.0 ± 5.2	46.7 ± 5.6	17.4 ± 0.2	1.8	0.7
1	>100	58.3 ± 11.5	>100	94.1 ± 4.8	44.9 ± 23.9	35.0 ± 15.5	61.1 ± 15.9	66.6 ± 17.6	1.1	1.1
2	13.3 ± 0.1	10.5 ± 1.5	>100	49.8 ± 2.7	26.5 ± 2.7	23.1 ± 3.9	46.7 ± 3.5	9.7 ± 2.5	4.5	0.9
3	12.5 ± 2.9	2.6 ± 0.01	90.3 ± 3.3	34.2 ± 3.0	33.2 ± 13.5	23.6 ± 6.8	44.6 ± 0.6	10.9 ± 0.5	17.2	4.2
4	20.9 ± 5.3	19.9 ± 0.4	87.5 ± 7.9	45.3 ± 4.3	37.8 ± 1.3	28.4 ± 10.9	23.5 ± 1.8	15.1 ± 1.0	1.2	0.8
5	0.5 ± 0.1	0.08 ± 0.01	4.2 ± 0.1	0.07 ± 0.002	6.3 ± 0.2	1.2 ± 0.6	2.5 ± 0.2	1.5 ± 0.3	31.3	18.8
6	0.5 ± 0.1	0.09 ± 0.01	7.1 ± 1.7	0.06 ± 0.005	12.0 ± 3.2	3.8 ± 1.7	3.2 ± 0.8	1.1 ± 0.02	35.6	12.2
7	0.6 ± 0.1	0.37 ± 0.04	7.6 ± 0.9	0.06 ± 0.001	2.2 ± 0.04	0.3 ± 0.1	3.1 ± 0.3	1.0 ± 0.01	8.4	2.7
Combo[d]	18.7 ± 5.6	14.8 ± 0.9	27.8 ± 1.1	12.9 ± 1.7	28.0 ± 2.9	5.7 ± 2.3	9.8 ± 2.0	38.6 ± 5.0	0.7	2.6
Combo[e]	13.8 ± 1.8	12.0 ± 0.7	28.4 ± 1.8	11.8 ± 1.6	28.9 ± 0.1	10.8 ± 0.7	8.6 ± 2.1	38.4 ± 0.6	0.7	3.2
Combo[f]	19.2 ± 2.5	15.2 ± 1.1	28.6 ± 2.9	10.1 ± 0.7	40.9 ± 0.6	13.5 ± 0.2	6.4 ± 0.4	28.9 ± 0.1	0.4	1.9
Combo[g]	16.1 ± 1.8	12.7 ± 0.1	22.8 ± 2.5	7.8 ± 0.6	18.4 ± 8.2	5.8 ± 0.4	7.3 ± 1.4	33.5 ± 9.8	0.6	2.6
Combo[h]	11.9 ± 2.2	10.9 ± 1.6	25.9 ± 1.0	9.0 ± 1.1	12.4 ± 0.2	4.7 ± 0.4	6.3 ± 1.1	27.3 ± 0.6	0.6	2.5
Combo[i]	16.4 ± 0.9	13.3 ± 0.3	23.2 ± 3.2	8.0 ± 0.2	23.2 ± 4.6	11.8 ± 4.8	5.7 ± 0.2	20.4 ± 7.1	0.4	1.5

[a]Data represent the mean ± standard deviation (SD) of three replicates [b]SI, selectivity index, IC_{50} (in HUVEC)/IC_{50} (in MCF-7). [c]SI, selectivity index, IC_{50} (in HK2)/IC_{50} (in MCF-7). [d]Combo, the equimolar mixture of OXA and CA. [e]Combo, the equimolar mixture of OXA and FA. [f]Combo, the equimolar mixture of OXA and CB. [g]Combo, OXA and CA are mixed in a molar ratio of 1:2. [h]Combo, OXA and FA are mixed in a molar ratio of 1:2. [i]Combo, OXA and CB are mixed in a molar ratio of 1:2.

suggests that fibrates possess multifaceted potential in oncology: (i) fibrates can significantly induce ERS in cancer cells and promote ROS generation[26−28] and (ii) fibrates can profoundly influence cholesterol metabolism through multiple mechanisms, including enhancing high-density lipoprotein (HDL) synthesis, upregulating ATP-binding cassette transporter A1 (ABCA1) expression, facilitating reverse cholesterol transport, and mediating antitumor immune responses.[25,29] A preclinical study in MC38 colon tumor-bearing mice demonstrated that the PPAR agonist could enhance fatty acid oxidation and significantly increase both the number and activity of $CD8^+$ T lymphocytes in the TME.[30] Nevertheless, how to effectively integrate the metabolic regulation and ERS-inducing functions of fibrates into antitumor strategies and achieve synergistic effects with chemotherapy has become a focal area of intensive research interest.

Platinum (Pt)-based drugs are among the most widely used chemotherapeutics, incorporated into approximately 50% of chemo-regimens administered in the clinic.[31] These agents exert their effects primarily through the formation of platinum-DNA adducts, which interfere with DNA replication and transcription, ultimately leading to apoptosis in cancer cells.[31] However, the severe systemic toxicity caused by poor solubility and selectivity limits the clinical therapeutic effect. In recent years, the combination of fibrates and Pt(IV) scaffolds has emerged as a promising strategy. Wang, Sun, and Guo et al. developed the lipophilic fenofibrate-Pt(IV) complexes, which reversed platinum resistance and enhanced therapeutic efficacy through dual mechanisms involving lipid metabolism disruption and ferroptosis induction.[32−34] Qiao et al. developed cisplatin-like bezafibrate-Pt(IV) prodrugs, which achieved the synergistic anticancer effect of metabolic regulation and DNA damage by targeting the ROS-AMPK pathway.[35] Moreover, cisplatin-like gemfibrozil-Pt(IV) prodrugs have been proven to enhance the effectiveness of both starvation therapy and chemotherapy.[36] However, cisplatin fails to trigger effective ICD because it cannot induce CRT exposure on the cell surface.[37] Notably, the third-generation Pt compound oxaliplatin (OXA) demonstrates notable efficacy against various solid tumors and was the first Pt-based agent to be confirmed as capable of inducing ICD.[6] However, the efficacy of OXA-induced ICD is still significantly constrained by the immunosuppressive nature of tumor microenvironment (TME).[38,39] In this regard, we wonder whether rational modulation of the tumor immune microenvironment could enhance the effectiveness of the OXA-induced ICD.

In order to modulate the tumor immune microenvironment and achieve an enhanced cancer chemoimmunotherapy, we perform molecular-level coupling of the oxaliplatin(IV) scaffold with fibrates and synthesize a series of fibrate-oxaliplatin(IV) conjugates (compounds **2**−**7** in Figure 1). The cell and molecular biology techniques were employed to elucidate the underlying molecular mechanisms of this synergistic interaction (Scheme 1). Specifically, fibrate-mediated activation of the PPARα signaling pathway and remodeling of the immunosuppressive TMEs were investigated. Finally, the anticancer efficacy and systemic toxicity of these prodrug molecules were evaluated in a tumor-bearing mouse model.

2. RESULTS AND DISCUSSION

2.1. Synthesis and Characterization. The synthetic pathways leading to compounds **1**−**7** are illustrated in Figure 1. Pt(IV) intermediate **1** was synthesized by oxidizing OXA with hydrogen peroxide (H_2O_2), and its structure was characterized through infrared spectroscopy (IR) and ultra-high-resolution Fourier transform mass spectrometry (FTMS). Clofibric acid (CA), fenofibric acid (FA), and cyclopentetic acid (CB) are the active metabolites of clofibrate, fenofibrate, and ciprofibrate, respectively, and possess enhanced pharmacokinetic properties.[40] Therefore, these three fibrate metabolites were selected as ligands for the synthesis of fibrate-oxaliplatin(IV) conjugates. The CA-NHS ester synthesized

https://doi.org/10.1021/acs.jmedchem.5c02436
J. Med. Chem. 2025, 68, 26328−26347

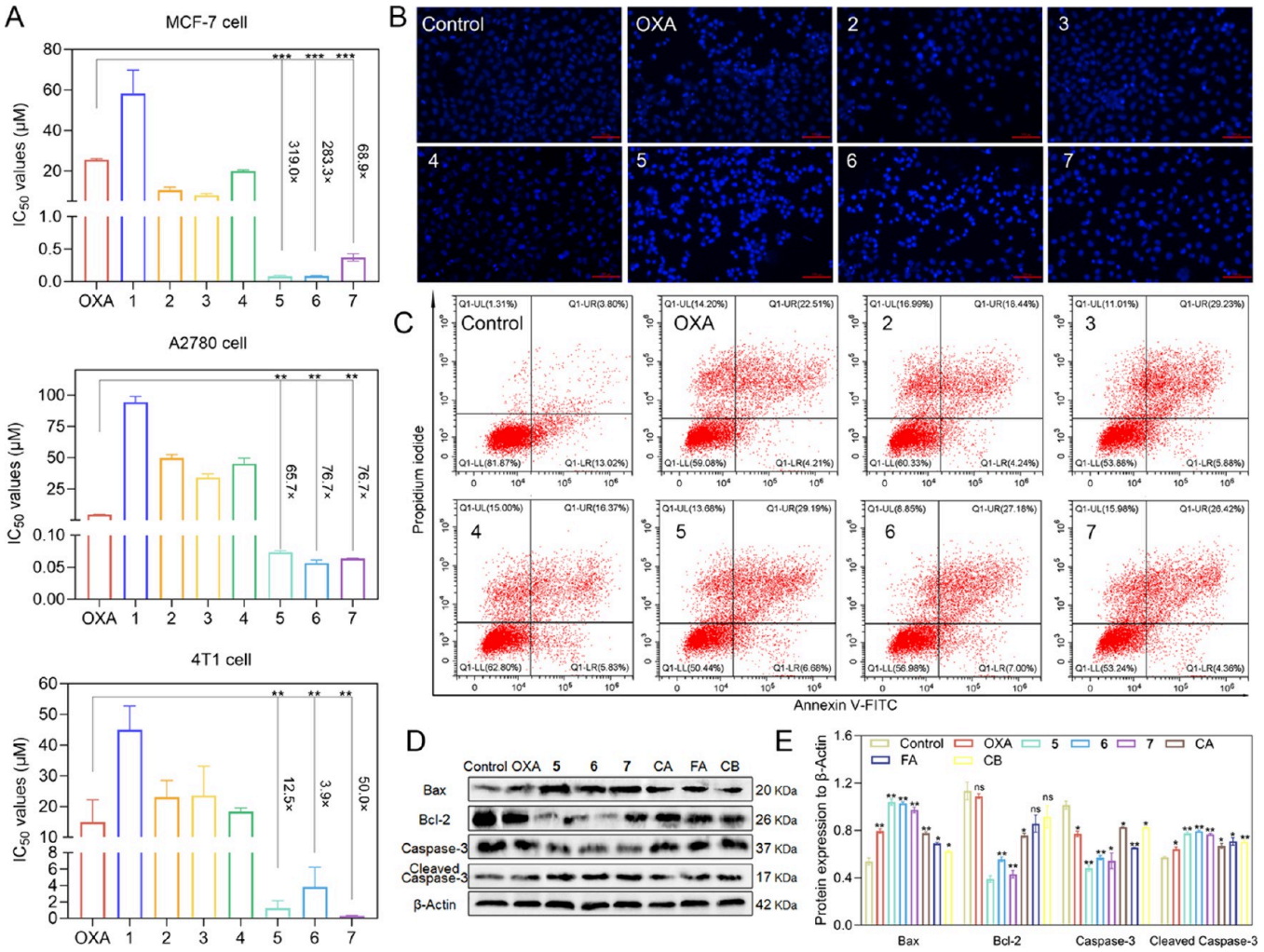

Figure 2. Cytotoxicity of the compounds. (A) The IC_{50} values of OXA and compounds **1**−**7** for 72 h in A2780, MCF-7, and 4T1, respectively. (B) Hoechst 33342 staining of MCF-7 cells exposed to compounds at 5 μM for 24 h. (C) Flow cytometry analysis of MCF-7 cells treated with compounds at 2.5 μM for 36 h. (D) Expression of Bax, Bcl-2, cleaved caspase-3, and caspase-3 in MCF-7 cells after treatment with compounds. (E) Gray values of Bax, Bcl-2, cleaved caspase-3, and caspase-3 compared with β-actin, respectively. ***$P < 0.001$, **$P < 0.01$, *$P < 0.05$, ns indicates no statistical significance.

following the literature procedure.[41] The monosubstituted compounds **2**−**4** were synthesized by reacting CA-NHS, FA, or CB with compound **1** in a dimethyl sulfoxide (DMSO) solution containing triethylamine (TEA) and O-benzotriazole-*N*,*N*,*N*′,*N*′-tetramethylurea tetrafluoroborate (TBTU), respectively. The disubstituted compounds **5**−**7** were synthesized by reacting compound **1** with CA, FA, or CB in an *N*,*N*-dimethylformamide (DMF) solution containing TEA and TBTU, respectively, under a nitrogen atmosphere. All fibrate-oxaliplatin(IV) conjugates were characterized by $^{1}H/^{13}C$ NMR, FTMS, bidimensional NMR (HMBC), ^{195}Pt-NMR, and elemental analysis. All compounds are >95% pure by high-performance liquid chromatography (HPLC) analysis. The stability of compounds **2**-**7** was further verified, and all relevant data are provided in the Supporting Information files (Figures S1−S39).

2.2. Cytotoxicity Effects of Compounds. The cytotoxicity of compounds was assessed against cancer cell lines (A2780, MCF-7, and 4T1) and normal cell models (HUVEC, HK2) using the 3-(4, 5-dimethylthiazole-2-yl)-2,5-diphenyltetrazolium bromide (MTT) colorimetric method. Monotherapy of OXA, CA, FA, CB, and **1** and combined therapy of ligands + OXA (Combo groups) were used as positive controls. The half-maximal inhibitory concentration (IC_{50}) values are summarized in Table 1. After 24 h of treatment, all synthetic compounds exhibited a consistent pattern of concentration-dependent cytotoxicity. Pt(IV) compounds **2**−**7** exhibited significantly enhanced cytotoxic effects compared to OXA, compound **1**, fibrate metabolites, and all combo groups. Moreover, a clear trend was observed, showing that disubstituted derivatives exhibited a greater cytotoxic potency than their monosubstituted derivatives. Specifically, after 24 h of treatment, the IC_{50} values of compounds **5**−**7** in MCF-7 cells were 0.5 ± 0.1, 0.5 ± 0.1, and 0.6 ± 0.1 μM, respectively, which were markedly lower than that of OXA (51.9 ± 13.2 μM). Upon extending the exposure time to 72 h, compounds **5**−**7** demonstrated nanomolar IC_{50} values in MCF-7 cells, ranging from 80 to 370 nM. As shown in Figure 2A, compounds **5**−**7** showed up to approximately 319-fold greater potency compared to that of OXA (25.5 ± 0.5 μM). Importantly, the cytotoxic selectivity indexes (SI^a = IC_{50} in HUVEC/IC_{50} in MCF-7) of **5**−**7** were 31.3, 35.6, and 8.4, respectively, which also were higher than that of OXA (1.8). In addition, nephrotoxicity is a typical adverse effect associated

https://doi.org/10.1021/acs.jmedchem.5c02436
J. Med. Chem. 2025, 68, 26328−26347

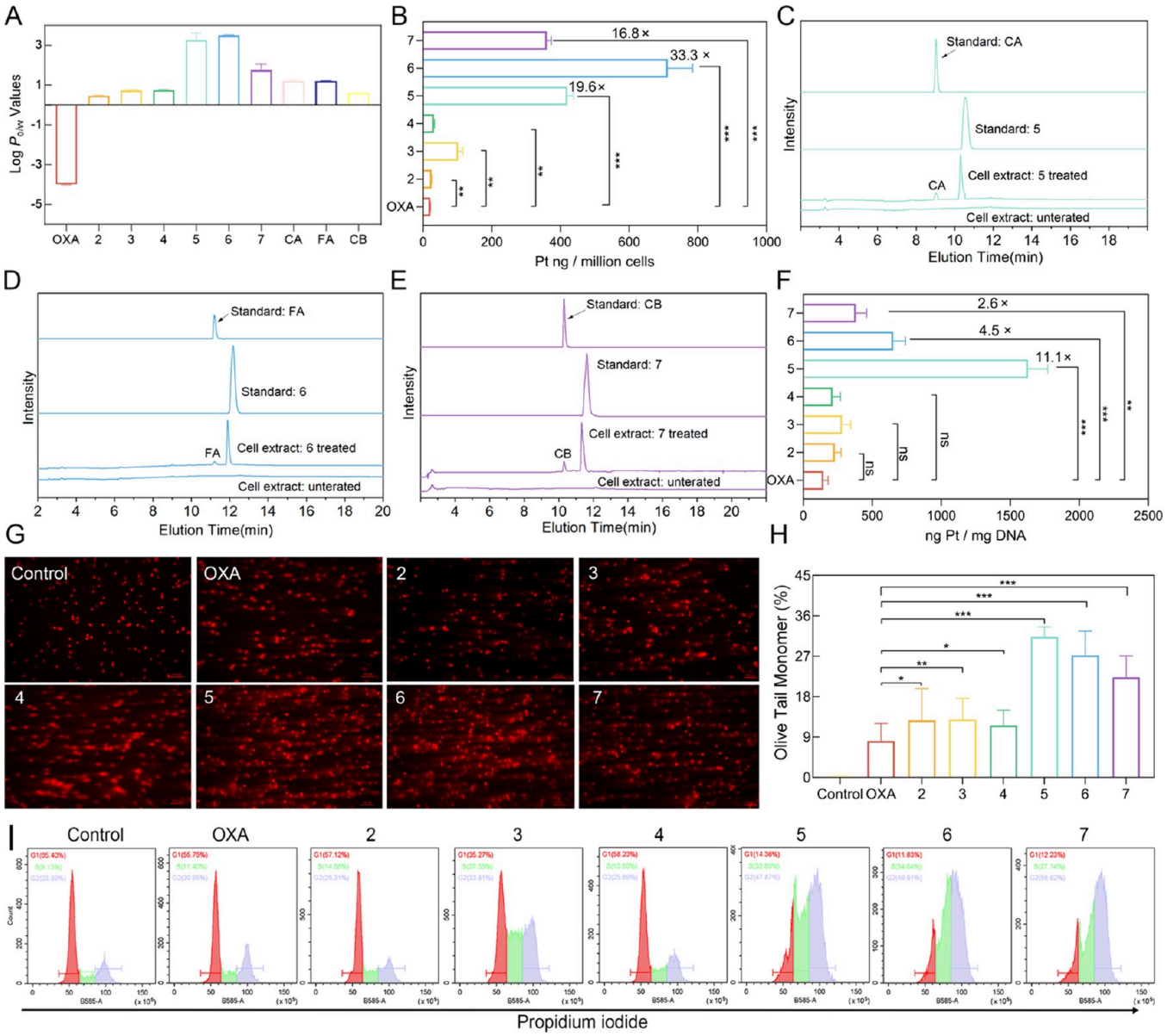

Figure 3. Pt content and DNA damage. (A) Log $P_{o/w}$ values of compounds. (B) Pt content of MCF-7 cells after treatment with compounds. (C–E) The reduction status of MCF-7 in cells after treatment with compounds **5**–**7** (100 μM) for 3 h, respectively. (F) Pt-DNA content in MCF-7 cells. (G) Fluorescence images of DNA damage. (H) "Olive tail moment" statistics. (I) Detection of DNA content by flow cytometry. ***P < 0.001, **P < 0.01, *P < 0.05, ns indicates no statistical significance.

with Pt-based chemotherapeutics. Compounds **5**–**7** showed SI^b values in HK2 cells that were 3.9 to 26.9 times higher than that of OXA, indicating a potentially improved safety profile. Besides, in the OXA-resistant cell line (MCF-7/OXA), the IC_{50} values of compounds **5**–**7** were 0.10 ± 0.02, 0.17 ± 0.04, and 0.7 ± 0.1 μM, respectively, which were significantly lower than that of the OXA group (87.4 ± 4.7 μM). In terms of the resistance index (RI), the RI of OXA was 3.4, while the RI values of compounds **5**–**7** did not exceed 2.0 (Table S1). Particularly, the cytotoxicity of compound **5** showed no significant change in the MCF-7 and MCF-7/OXA cells. These results indicated that the fibrate-oxaliplatin(IV) conjugates can partially reverse the resistance of MCF-7 cells to OXA. Based on these findings, the MCF-7 cell line was selected as the representative model for subsequent *in vivo* and *in vitro* studies.

To further evaluate the cytotoxic effects of these Pt(IV) compounds, Hoechst 33342 staining and Annexin V-FITC/PI double staining flow cytometry assays were conducted. As shown in Figure 2B and Figure S40, after 24 h of treatment, bright, dense, and high-intensity blue fluorescent plaques appeared in the nuclei of the compound-treated groups compared with the control group. Especially in the compound **5**–**7** treatment groups, obvious nuclear concentration and nuclear fragmentation phenomena were also observed. The quantitative flow cytometry analysis showed that compared with control (18.1%) and the group with the highest concentration of OXA (40.9%), compounds **2**–**7** significantly increased the proportion of cell death after 36 h of treatment (Figure 2C and Figure S41). The cell mortality rates of **5**–**7** treatment groups were 49.6, 43.0, and 46.8%, respectively. Western blot results shown in Figure 2D,E also indicated that compared with control, the expression of the pro-apoptotic protein Bax was significantly upregulated in the cells treated with compounds **5**–**7**, whereas the expression of the

https://doi.org/10.1021/acs.jmedchem.5c02436
J. Med. Chem. 2025, 68, 26328−26347

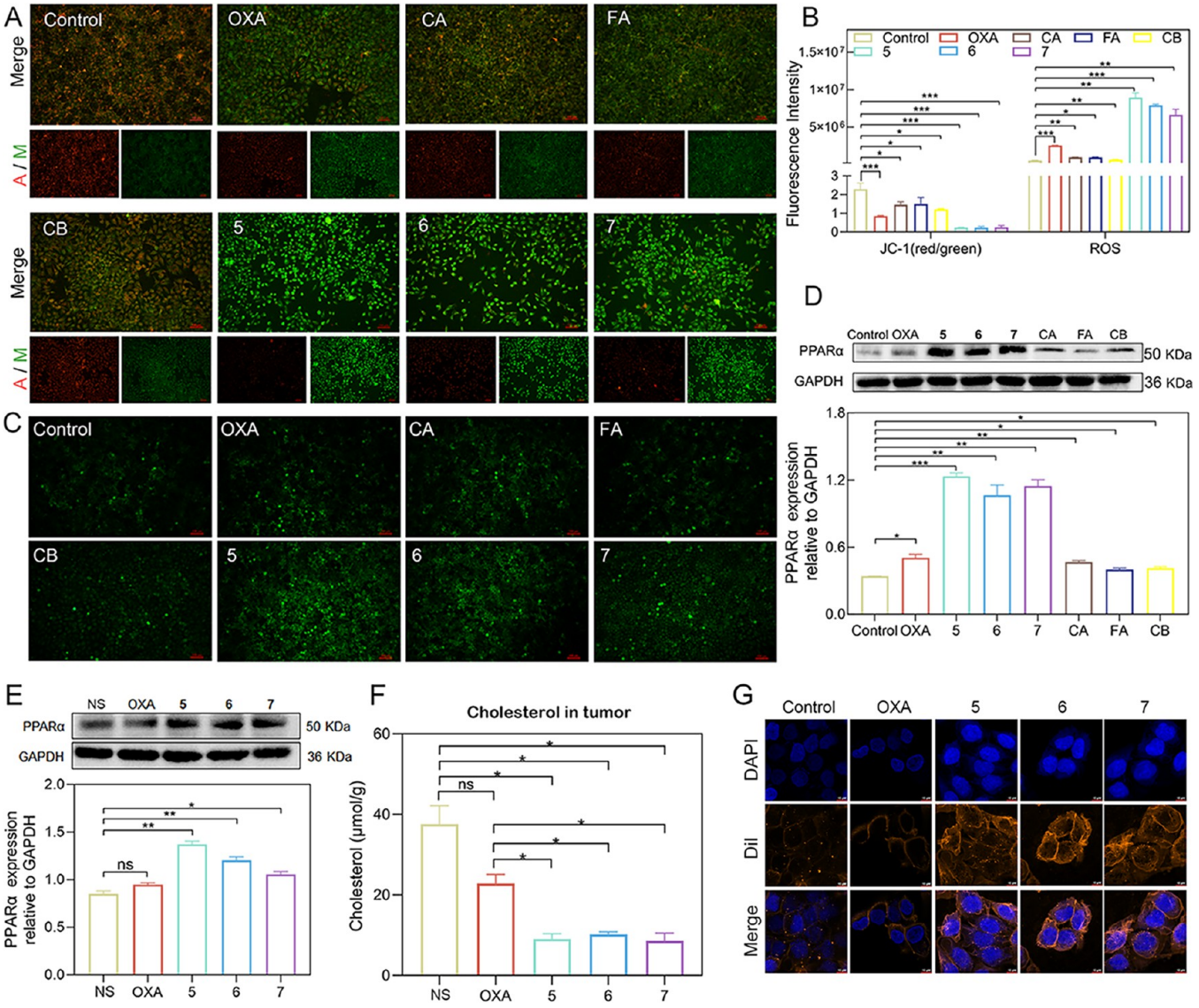

Figure 4. Mitochondrial dysfunction, ROS generation, cholesterol content, and ERS. (A) JC-1 staining image of MCF-7 cells. M stands for JC-1 monomer (green) and A stands for JC-1 aggregate (red). (B) Quantification of fluorescence intensity. (C) DCFH-DA staining of MCF-7 cells. (D) Expression of PPARα in MCF-7 cells after 24 h of drug treatment and gray value statistics of PPARα and GAPDH. (E) Expression of PPARα in tumors and gray value statistics of PPARα and GAPDH. NS means the normal saline group. (F) Cholesterol content in tumor tissue. (G) Fluorescence images of MCF-7 cells treated with compounds for 12 h and stained with Dil (red, cell membrane) or DAPI (blue, cell nucleus). ***P < 0.001, **P < 0.01, *P < 0.05, ns indicates no statistical significance.

antiapoptotic protein Bcl-2 was downregulated, with effects superior to those observed in the OXA and ligand treatment groups. Caspase-3 is a crucial downstream effector in the apoptotic signaling pathway, and the activation of cleaved caspase-3 serves as a key indicator of irreversible apoptosis.[42] The experimental results demonstrated that the expression of caspase-3 protein was downregulated, while the expression of cleaved caspase-3 was significantly upregulated. In brief, these findings have preliminarily validated the feasibility of fibrate metabolite-modified oxaliplatin-like Pt(IV) prodrugs in enhancing the antitumor efficacy of chemotherapy.

2.3. Drug Accumulation, Reduction Behavior, and DNA Damage. Improving the transmembrane transport efficiency is essential for enhancing the antitumor activity of Pt-based drugs. In particular, the lipid−water partition coefficient is regarded as an important factor influencing drug intake. In recent years, accumulating evidence has indicated that incorporating ligands into Pt(IV) scaffolds can effectively enhance drug lipophilicity.[43] To explore the reasons why fibrate-oxaliplatin(IV) conjugates, particularly the disubstituted derivatives **5**−**7**, exhibit superior anticancer activities compared to OXA, the Log $P_{o/w}$ values of these compounds were determined using the shake-flask method. As shown in Figure 3A, the Log $P_{o/w}$ values of all Pt(IV) compounds were higher than that of OXA (−4.0 ± 0.04), and the disubstituted derivatives **5**−**7** display values exceeding 1.5. Subsequently, intracellular Pt content was quantitatively analyzed by ICP-MS. The results showed that after 8 h of treatment, the Pt content in all Pt(IV) compound-treated groups was higher than that in OXA, and the disubstituted compounds exhibited significantly greater cellular uptake than monosubstituted ones. Specifically, the Pt content following treatment with compound **5** (419.9 ± 18.0 ng Pt/million cells), compound **6** (712.4 ± 72.8 ng Pt/million cells), and

https://doi.org/10.1021/acs.jmedchem.5c02436
J. Med. Chem. 2025, 68, 26328−26347

compound 7 (360.5 ± 13.0 ng Pt/million cells) was markedly higher than that in the OXA-treated group (21.4 ± 0.4 ng Pt/million cells), representing increases of 19.6-, 33.3-, and 16.8-fold, respectively (Figure 3B). These findings confirm that enhanced lipophilicity promotes the intracellular Pt accumulation and is one important factor for the superior cytotoxicity of disubstituted compounds compared to that of OXA and monosubstituted ones.

The reduction-activation process of Pt(IV) compounds is another critical factor that influences their cytotoxic effects. Typically, kinetically inert Pt(IV) compounds require stimulation by high intracellular concentrations of reductants to release axial ligands and the active Pt(II) core.[31] Therefore, the reduction behavior of the Pt(IV) compounds was systematically investigated. Cyclic voltammetry (CV) analysis revealed that the reduction potentials of compounds **2**−**7** were −0.8, −0.8, −0.7, −0.8, −0.8, and −0.8 V, respectively (vs saturated calomel electrode), with irreversible reduction peaks observed (Figure S42). These results revealed that the compounds possess irreversible reduction characteristics. Furthermore, a phosphate buffer solution (PBS) containing ascorbic acid (AsA) or glutathione (GSH) was used to simulate TME and coincubated with these compounds at 37 °C in the dark.[44] During incubation, HPLC was employed to detect the release of the ligands. Results shown in Figures S43 and S44 demonstrate that in the presence of AsA, the monosubstituted compounds **2**−**4** exhibited significantly higher reduction rates, whereas the disubstituted compounds **5**−**7** remained largely unchanged. However, it is important to note that the reducing environment within tumor cells is considerably more complex than that simulated by the simple addition of GSH or AsA to buffer solutions. To further evaluate the reduction behavior of the disubstituted compounds under biologically relevant conditions, cell lysates were collected and analyzed after treatment with compounds **5**−**7** for 3 h, respectively. As shown in Figure 3C−E, distinct peaks corresponding to the released ligands and the original compounds were observed. Notably, after coincubation with plasma at 37 °C in the dark for 72 h, no decomposition peaks were observed for compounds **5**−**7**, which retained their structural integrity (Figure S45). These results indicate that the fibrate-oxaliplatin(IV) conjugates can be selectively activated in TME and are prone to release the effector Pt(II) species and axial ligands, thereby exerting cytotoxic effects.

It is well known that Pt(II) drugs primarily exert their biological effects by forming highly reactive cross-links with genomic DNA.[45] To investigate the intrinsic correlation between the reductive activation process and the cytotoxicity of Pt(IV) compounds, the intracellular DNA platinization content was assessed. ICP-MS analysis (Figure 3F) showed that after 8 h of incubation, the amount of platinized DNA increased in all treatment groups. Although there was no significant difference between the single substituents and OXA, the number values of Pt-DNA in compounds **2**−**4** was still slightly higher than that in OXA. Notably, the platinized DNA content in the compound **5**−**7** treatment groups was 11.1-, 4.5-, and 2.6-fold higher, respectively, than that in the OXA group (146.6 ± 33.6 ng Pt/mg DNA). This result indicated that the Pt(IV) compounds have a stronger DNA binding capacity within cells and further supported the earlier findings on cellular uptake. To visually evaluate the extent of DNA damage, a comet assay was conducted. As shown in Figure 3G,H, compared with the intact nuclear morphology observed in the control group, the Pt(IV) compound treatment groups exhibited evident DNA fragmentation, characterized by longer tail lengths than those in the OXA group. Particularly, the compound **5**−**7** treatment groups induced the longest "Olive" tailing, indicating more pronounced DNA damage. Such DNA damage usually activates cell cycle checkpoints and leads to cycle arrest.[45] Here, we further analyzed changes in the cell cycle distribution using flow cytometry. As illustrated in Figure 3I and Figure S46, compared with the control, OXA, and fibrate groups, the Pt(IV) compound-treated groups exhibited significant G2/M phase arrest, with the most pronounced effects observed in the disubstituted compound groups. In summary, these findings suggest that Pt(IV) compounds, especially compounds **5**−**7**, exert potent antitumor activity by binding to DNA and inducing damages.

2.4. Mitochondrial Dysfunction, ROS Generation, Cholesterol Inhibition, and ERS Form a Vicious Cycle. Mitochondrial dysfunction represents a critical mechanism through which OXA induces apoptosis.[46] Accumulating evidence suggests that OXA can disrupt mitochondrial function by directly damaging mitochondrial DNA, inducing oxidative stress, and interfering with calcium homeostasis etc.[46] A notable early indicator of apoptosis is the reduction of the mitochondrial membrane potential ($\Delta\Psi$m). To evaluate changes in $\Delta\Psi$m, a JC-1 fluorescent probe was used for detection. As shown in Figure 4A and Figure S47A, the red fluorescence of the cells treated with compounds **2**−**7** was significantly decreased, while the green fluorescence increased correspondingly. Quantitative analysis of fluorescence intensity further revealed that the aggregate/monomer ratio was significantly lower in the compound-treated groups compared to the control, suggesting impaired mitochondrial function (Figure 4B and Figure S47C).

As the primary source of ROS in eukaryotic cells, mitochondria play a central role in oxidative stress under dysfunctional conditions, which is characterized by excessive ROS accumulation.[47] When ROS levels surpass the capacity of cellular antioxidant defense, oxidative stress occurs, leading to damage to biological macromolecules such as lipids, proteins, and DNA, and ultimately culminating in cell death.[48] Notably, the axial ligand fibrates can also indirectly enhance ROS production by activating the PPARα signaling pathway and upregulating the expression of peroxisomal acyl-CoA oxidase 1 (ACOX1).[26−28] Therefore, the ROS level in cells after drug treatment was assessed using the DCFH-DA probe. As shown in Figure 4C and Figure S47B, green fluorescence signals were markedly increased in the OXA or fibrate monotherapy groups compared to the control, indicating that both treatments can induce ROS generation. However, the compound **2**−**7** treatment groups significantly increased the ROS level at the same concentration, with fluorescence intensity much higher than that of other groups ($P < 0.001$, Figure 4B and Figure S47D). These results indicate that Pt(IV) compounds **2**−**7** exacerbate oxidative stress, thereby enhancing the cytotoxicity.

Activation of PPARα also promotes reverse cholesterol transport, enhances bile acid synthesis, inhibits *de novo* cholesterol synthesis, promotes fatty acid oxidation, regulates lipoprotein metabolism, and significantly reduces cholesterol levels.[26,28] Western blot results showed that the PPARα expression was markedly upregulated both *in vivo* and *in vitro* in compounds **5**−**7** treatment groups (Figure 4D,E), which was accompanied by a significant reduction in cholesterol content in tumor tissues (Figure 4F). Further blood

https://doi.org/10.1021/acs.jmedchem.5c02436
J. Med. Chem. 2025, 68, 26328−26347

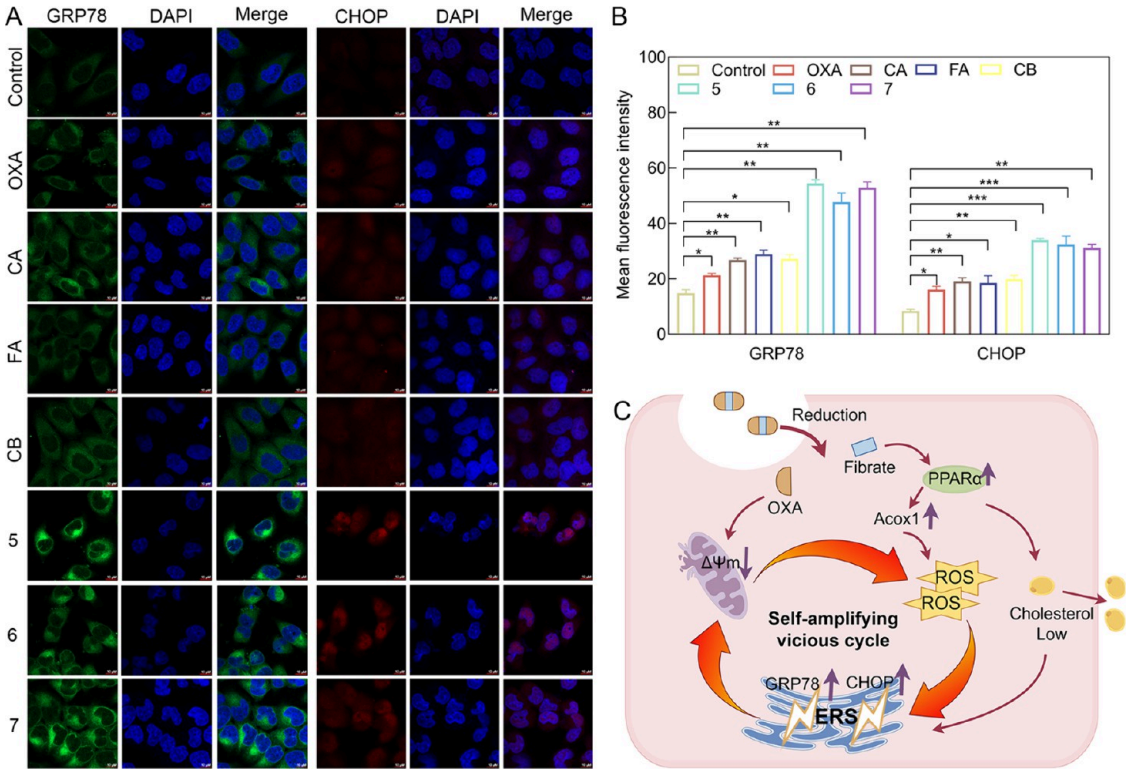

Figure 5. Potential mechanisms triggering ERS. (A) Imaging of GRP78 and CHOP expression in MCF-7 cells after exposure to compounds (5 μM) for 24 h, respectively. Single-image planes of Alexa Fluor 488/594-conjugated goat antirabbit IgG (H+L) (green/red), DAPI (blue), and merged green/red and blue channels are displayed. (B). Quantification of the mean fluorescence value of GRP78 and CHOP. (C) Diagram of the potential mechanisms that trigger ERS. ***P < 0.001, **P < 0.01, *P < 0.05.

cholesterol content tests (Figure S48) revealed no significant difference between the compound **5**−**7** treatment group and the control group, suggesting that compounds **5**−**7** may primarily regulate cholesterol levels in tumor tissues without exerting notable effects on normal tissues. As a critical component of cellular membranes, cholesterol plays a pivotal role in maintaining membrane integrity. Cholesterol depletion leads to elevated membrane tension, altered membrane fluidity, and ultimately cell lysis.[49] To evaluate whether the reduction in cholesterol levels is sufficient to modulate cancer cell activity, we performed additional experiments under controlled cholesterol conditions. As shown in Figure S49, exogenous cholesterol supplementation increased cell viability, particularly in the high-dose group. Dil staining revealed that the red fluorescence was predominantly localized to the cell membrane in the control, OXA, suggesting intact cellular membranes. In contrast, fibrate and compound **2**−**7** treatment groups exhibited intracellular aggregation of fluorescence (Figure 4G and Figure S49), indicating that cholesterol depletion caused severe membrane disruption and subsequent cell death.

Cholesterol, as a core structural component of the ERS, not only maintains membrane stability through its rigid steroid ring structure but also forms specialized lipid microdomains by interacting with phospholipids such as phosphatidylcholine and sphingomyelin.[49] Research indicates that a substantial decrease in intracellular cholesterol levels triggers UPR, thereby inducing ERS.[20] Concurrently, excessive accumulation of ROS further exacerbates ERS.[50] Glucose-regulated protein 78 (GRP78) is a key endoplasmic reticulum chaperone protein that plays a core role in protein folding and ERS reactions.[51] C/EBP-homologous protein (CHOP), a transcription factor, is primarily involved in regulating cell proliferation, differentiation, and energy metabolism and serves as a critical mediator of ERS-induced apoptosis.[52] To evaluate ERS activation, we assessed the expression levels of GRP78 and CHOP. As shown in Figure 5A,B, compared with the control, OXA, and ligand treatment groups, GRP78 and CHOP expression levels were significantly elevated in the **5**−**7** treatment groups, and CHOP showed obvious nuclear aggregation, indicating that ERS was continuously activated. Additionally, ERS would further aggravate mitochondrial dysfunction. Thus, fibrate-oxaliplatin(IV) conjugates establish a "self-amplifying vicious cycle" by inducing mitochondrial dysfunction, promoting ROS burst, inhibiting cholesterol synthesis, and triggering ERS (Figure 5C).

2.5. Antitumor Immunity *In Vivo* and *In Vitro*. ERS has been established as a core regulatory mechanism of ICD under pathological conditions. During the process of ICD in tumor cells, ERS facilitates the release of DAMPs, thereby activating antitumor immune responses.[53] The above studies have demonstrated that fibrate-oxaliplatin(IV) conjugates possess potent ERS-inducing capabilities; however, their ability to induce effective ICD remains to be further validated. Here, the release of DAMPs was detected in both cultured cells and tumor tissues following the drug treatment. CRT, a multifunctional protein located in the endoplasmic reticulum, rapidly translocates to the cell surface when tumor cells undergo ICD. There, it functions as an "eat me" signal that promotes DCs phagocytosis of tumor cells and enhances tumor responsiveness to anticancer immunotherapy.[54] Immunofluorescence staining results (Figure 6A) showed that

https://doi.org/10.1021/acs.jmedchem.5c02436
J. Med. Chem. 2025, 68, 26328−26347

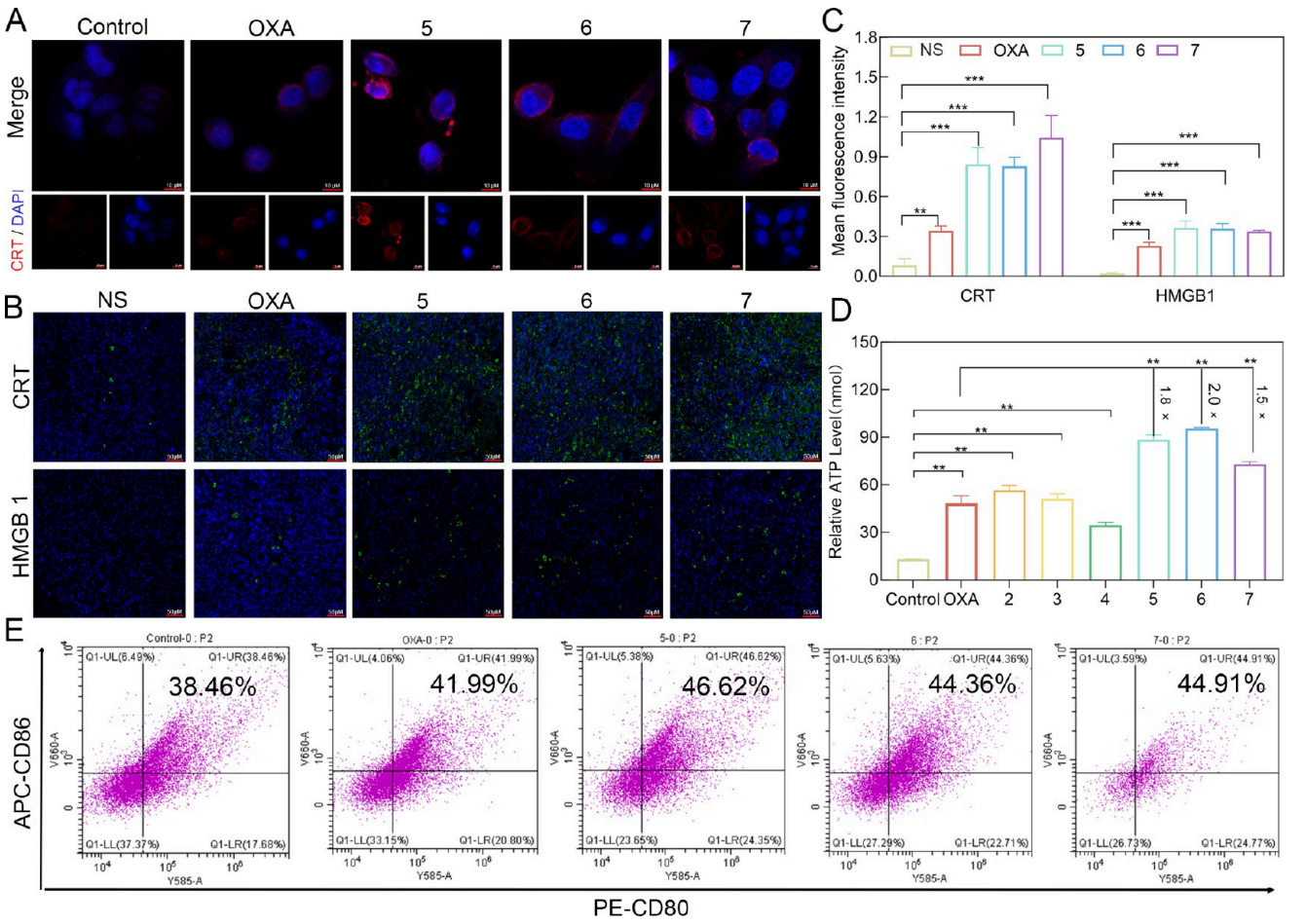

Figure 6. ICD induction. (A) Fluorescence images of CRT expression in MCF-7 cells after exposure to compounds (5 μM) for 24 h, respectively. Single-image planes of Alexa Fluor 594-conjugated goat antirabbit IgG (H+L) (red), DAPI (blue), and merged red and blue channels are displayed here. (B). Immunofluorescence staining of CRT and HMGB1 in tumor tissues. (C) Quantification of the mean fluorescence values of CRT and HMGB1. (D) The extracellular ATP level of MCF-7 cells. (E) Flow cytometry was used to detect the maturation of dendritic cells in tumor tissues (expression of $CD80^+$ and $CD86^+$ on $CD11c^+$ cells). ***$P < 0.001$, **$P < 0.01$, *$P < 0.05$.

compared with the control, the OXA-treated cells exhibited only a weak CRT signal, whereas the compound **5**−**7** treatment group showed a marked increase in CRT red fluorescence on the cell membrane surface. The immunohistochemical results of tumor tissues in Figure 6B were also consistent with the cellular-level CRT findings, confirming that compounds **5**−**7** effectively promoted CRT membrane translocation. The extracellular release of HMGB1 is a key step in ICD-mediated activation of antitumor immunity.[55] Tumor tissue section analysis (Figure 6B,C) showed that HMGB1 release was significantly enhanced in the compound **5**−**7** treatment groups compared to that in the OXA group. Additionally, ATP, a key "find-me" signaling molecule, plays a pivotal role in promoting DCs maturation and activation. As shown in Figure 6D, ATP release was significantly increased in the Pt(IV) compound treatment groups compared to the OXA group. Especially in the compound **5**−**7** treatment groups, the ATP levels increased by 1.8-, 2.0-, and 1.5-fold, respectively ($P < 0.001$). Furthermore, DAMPs released from dying cancer cells can enhance the maturation of DCs. Flow cytometry analysis (Figure 6E) demonstrated that compared with the NS group (38.5%) and the OXA group (42.0%), treatment with compounds **5**−**7** significantly increased the expression levels of DCs maturation markers CD80 and CD86. The proportions of $CD11c^+/CD80^+/CD86^+$ cells were 46.6, 44.4, and 44.9% in the respective groups. These results further confirm that compounds **5**−**7** have the ability to efficiently induce ICD and promote the maturation of DCs.

The tumor immunosuppressive microenvironment is also a critical factor that limits the amplification of the effects of ICD. It is well established that $CD8^+$ T cells serve as core effector cells in cancer immunotherapy. Specifically, $CD8^+$ T cells can directly lyse tumor cells by releasing cytotoxic molecules, such as granzyme and perforin. Additionally, they secrete IFN-γ, which upregulates the expression of major histocompatibility complex class I (MHC-I) molecules on tumor cells, thereby enhancing their susceptibility to immune-mediated destruction.[56] However, the functional activity of $CD8^+$ T cells are frequently suppressed within the TME. Notably, the accumulation of cholesterol in the TME has been identified as a key contributor to the functional exhaustion of $CD8^+$ T cells.[57] Therefore, modulating cholesterol metabolism represents a promising strategy for enhancing antitumor immune responses. The infiltration of $CD8^+$ T cells in tumor tissues from mice treated with various therapeutic agents was evaluated by using flow cytometry. As shown in Figure 7A,B, the $CD8^+$ T cell infiltration rates in the **5**−**7** treatment groups increased significantly to 26.3, 22.9, and 17.6%, respectively, which were markedly higher than those observed in the NS group (3.1%) and the OXA group (8.2%). Tissue section

https://doi.org/10.1021/acs.jmedchem.5c02436
J. Med. Chem. 2025, 68, 26328−26347

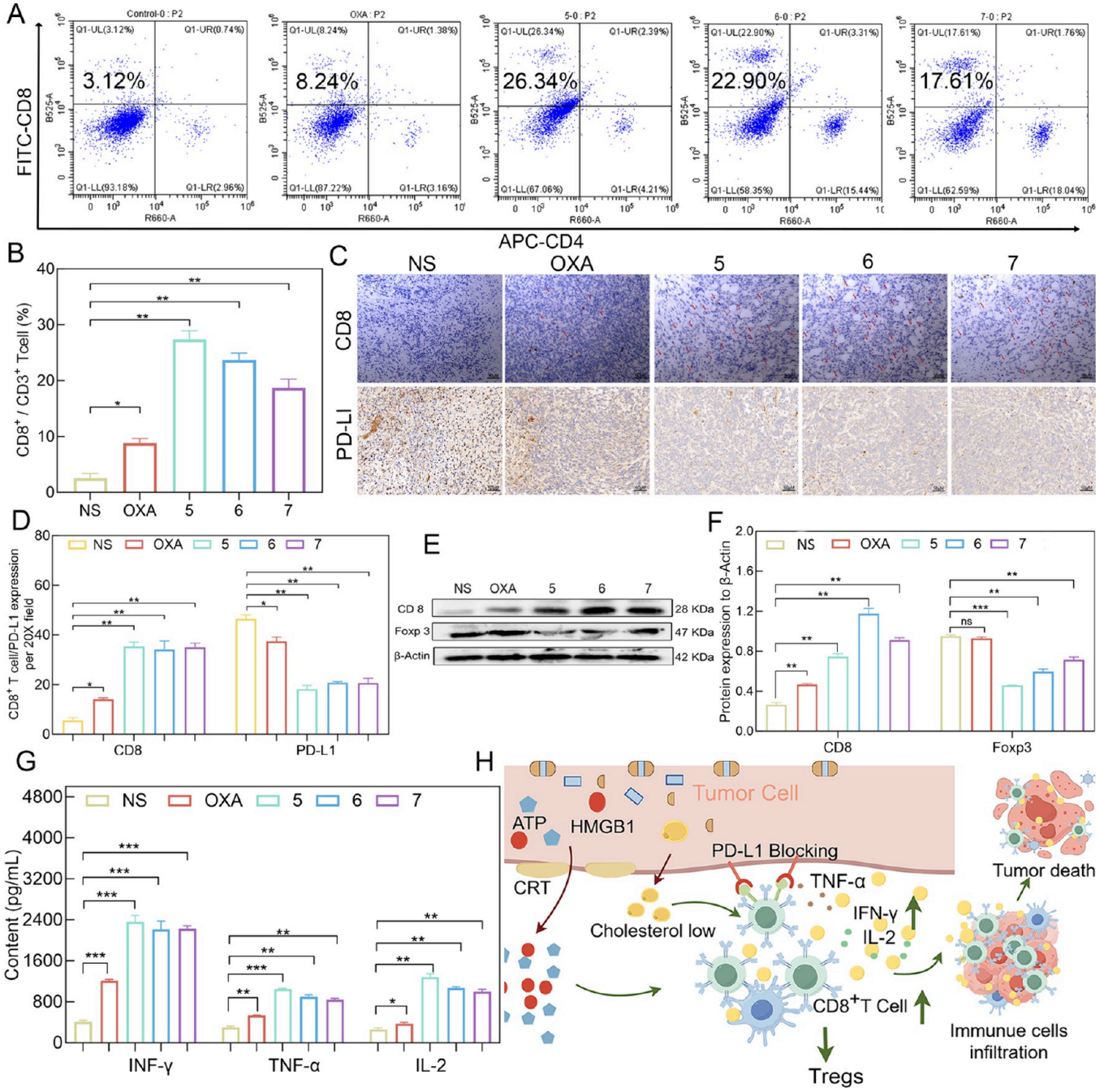

Figure 7. *In vivo* immunity. (A) Flow cytometry was used to detect the expression of $CD8^+$T in $CD3^+$T cells in the tumor tissues of each group. (B) The percentage of $CD8^+$T cells ($CD3^+CD8^+$) population. (C) The changes of CD8 and PD-L1 after 14 days of different treatments. (D) Quantification of CD8 and PD-L1. (E) Expression of CD8 and Foxp3 in tumor after drug treatment. (F) Gray value statistics of CD8/Foxp3 and β-actin in tumor tissues. (G) Content of IFN-γ, TNF-α, and IL-2 in the blood. (H) Fibrate-oxaliplatin(IV) conjugates exert the molecular mechanism of antitumor immunity. ***$P < 0.001$, **$P < 0.01$, *$P < 0.05$, ns indicates no statistical significance.

staining (Figure 7C,D) and Western blot analysis (Figure 7E,F) further confirmed that compared with the NS group, the expression of CD8 in tumor tissues was increased in the drug treatment group, particularly in the compound **5**−**7** treatment groups, where the effect was more pronounced than in the OXA group. This indicates a marked increase in the level of $CD8^+$ T cell infiltration into tumor tissues. Programmed death ligand-1 (PD-L1) is an immune checkpoint molecule that is highly expressed on the surface of tumor cells. Upon binding to programmed death receptor-1 (PD-1) on $CD8^+$ T cells, PD-L1 delivers inhibitory signals that suppress T cell activity.[58] Studies have demonstrated that cholesterol can directly interact with the transmembrane domain of PD-L1 via a cholesterol-recognition amino acid consensus (CRAC) motif, thereby stabilizing PD-L1 to prevent downstream degradation.[59] Thus, targeting cholesterol metabolism may serve as an effective approach to inhibiting the PD-1/PD-L1 signaling axis and restoring the functionality of exhausted $CD8^+$ T cells. Figure 7C,D demonstrates that the compound **5**−**7** treatment groups exhibited a more markedly inhibitory effect on PD-L1 expression compared to both the NS and OXA groups.

https://doi.org/10.1021/acs.jmedchem.5c02436
J. Med. Chem. 2025, 68, 26328−26347

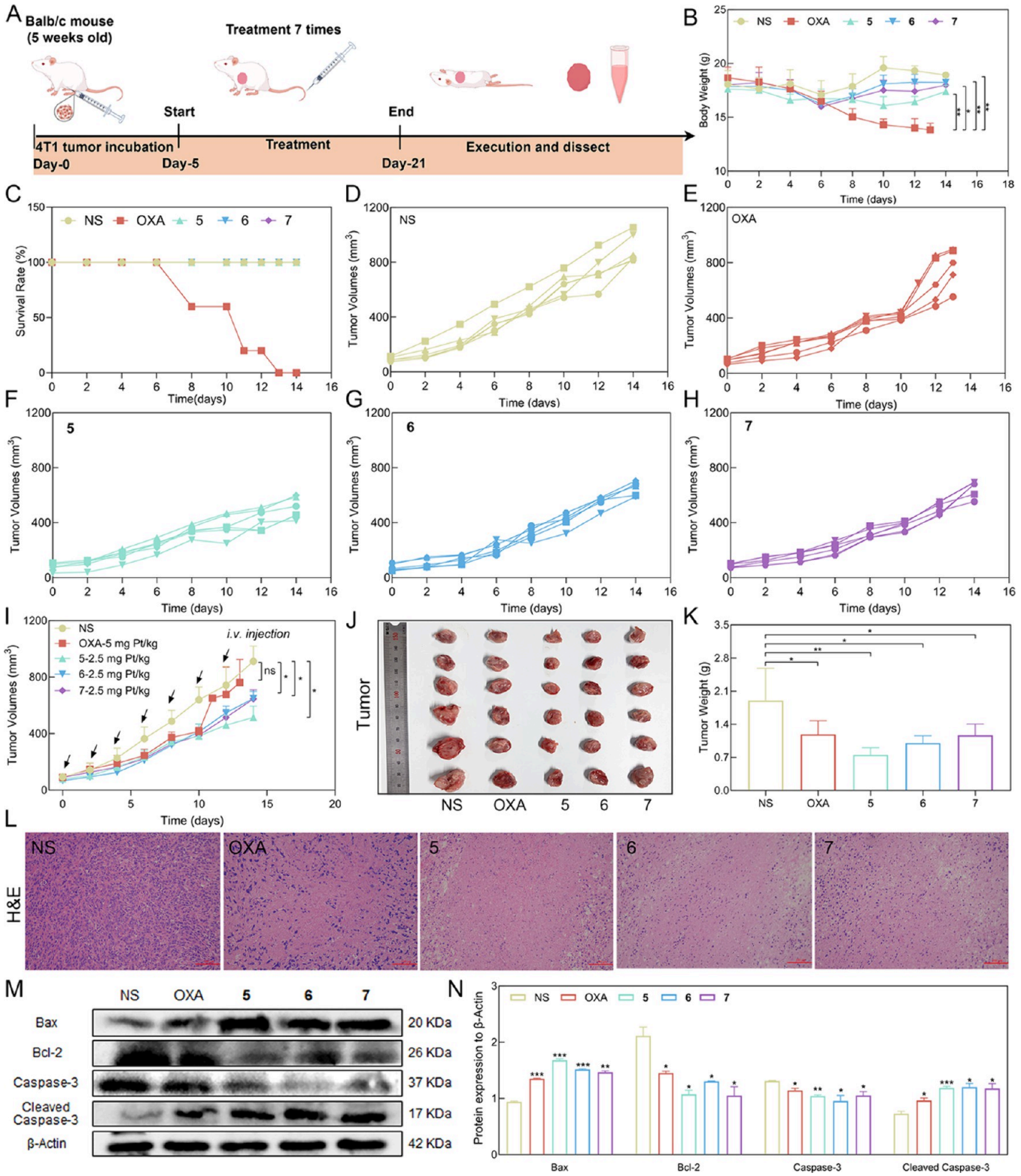

Figure 8. *In vivo* performance. (A) Diagram of the treatment plan for 4T1 tumors in Balb/c mice. (B) Body weight change chart of mice. (C) Survival rate of mice during treatment. (D–I) Tumor volume growth curves. (J) Tumor size map after treatment. (K) Tumor weight statistics after the end of treatment. (L) H&E staining of tumor tissues. (M) Expression of Bax, Bcl-2, cleaved caspase-3, and caspase-3 in tumor tissues. (N) Gray value statistics of Bax/Bcl-2/caspase-3/cleaved caspase-3 and β-actin in tumor tissues. ***$P < 0.001$, **$P < 0.01$, *$P < 0.05$, ns indicates no statistical significance.

Furthermore, regulatory T cells (Tregs) play a pivotal role in establishing and maintaining the immunosuppressive TME.[60] Forkhead box protein 3 (Foxp3) is a key transcription factor essential for the development and suppressive function of Tregs.[61] Loss of Foxp3 expression compromises Treg stability and function.[62] As illustrated in Figure 7E,F, the expression of

https://doi.org/10.1021/acs.jmedchem.5c02436
J. Med. Chem. 2025, 68, 26328−26347

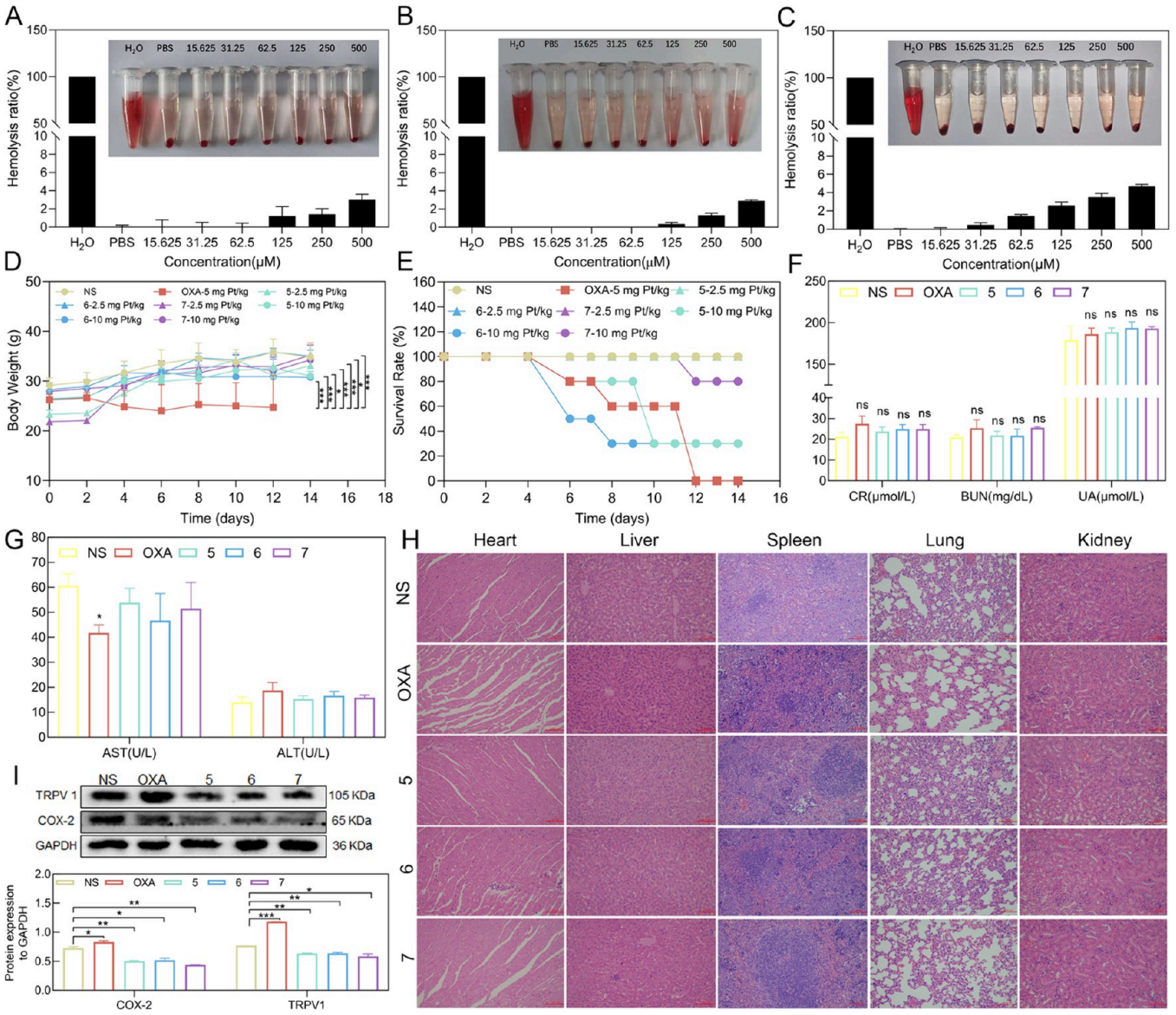

Figure 9. Biological safety evaluation. (A–C) Hemolysis test. (D) Body weight in acute toxicity test. (E) Survival curves of acute toxicity test. (F) Changes of CR, BUN, and UA in renal function of mice in the tumor suppression experiment. (G) Changes of AST and ALT in liver function of mice in the tumor suppression experiment. (I) Expression of COX-2 and TRPV1 in tumor tissues, along with the gray values statistics of COX-2/TRPV1 and GAPDH in tumor tissues. (H) H&E staining of the heart, liver, spleen, lung, and kidney of mice in the tumor suppression experiment. ***P < 0.001, **P < 0.01, *P < 0.05, ns indicates no statistical significance.

Foxp3 was significantly reduced in the compound **5**–**7** treatment groups compared with the NS and OXA groups. IFN-γ has been shown to induce a "fragility" state in Tregs within the TME, diminishing their immunosuppressive capacity and promoting further IFN-γ secretion.[63] ELISA results revealed that the serum IFN-γ levels in mice treated with compounds **5**–**7** were significantly higher than those in the NS and OXA groups (Figure 7G). In addition, in the **5**–**7** treatment groups, the levels of TNF-α (closely related to the toxic function of T cells) and IL-2 (promoting $CD8^+$ T cell infiltration) in the serum were also significantly increased (Figure 7G). In summary, in addition to effectively inducing ICD, fibrate-oxaliplatin(IV) conjugates can also remodel the immunosuppressive TME by blocking the PD-1/PD-L1 interaction, promoting the infiltration and functional recovery of cytotoxic $CD8^+$ T cells, attenuating Tregs-mediated immunosuppression, and enhancing IFN-γ production, thus exerting powerful antitumor effects (Figure 7H).

2.6. In Vivo Anticancer Performance. Based on the significant anticancer activity demonstrated above, we further evaluated the *in vivo* antitumor efficacy of the target compounds using a 4T1 tumor xenograft BALB/c nude mouse model. The administration protocol is illustrated in Figure 8A. When the tumor volume reached approximately 50~100 mm^3, the mice were randomly divided into five groups (n = 6): NS (normal saline), OXA (5 mg Pt/kg), **5** (2.5 mg Pt/kg), **6** (2.5 mg Pt/kg), and **7** (2.5 mg Pt/kg). Each group was administered via tail vein injection every 2 days for a total of seven doses. OXA is widely recognized for its severe side effects such as significant peripheral neurotoxicity and gastrointestinal reactions, which are major factors limiting its clinical application. Consequently, we closely monitored the physiological status of the mice throughout the experiment.

https://doi.org/10.1021/acs.jmedchem.5c02436
J. Med. Chem. 2025, 68, 26328–26347

During administration, the mice in compound **5**−**7** treatment groups exhibited physiological signs (mental state, activity level, feeding, and excretion) largely consistent with those of the NS group. Although the Pt(IV) compound treatment groups showed a slight decrease in body weight during the initial treatment phase, their weight gradually recovered later on, ultimately showing no statistically significant difference compared with the NS group (Figure 8B). In contrast, mice in the OXA treatment groups exhibited progressive weight loss throughout the treatment period and displayed signs of lethargy and listlessness. As shown in Figure 8B, after completing four treatments, two mice had weight loss that exceeded 20% of their initial weight. According to animal welfare standards, they are regarded as dead and the survival rate rapidly declined to 60%. The first mouse death occurs starting on day 11, and all mice in the OXA groups have died by day 13. Therefore, treatment was terminated on day 14, and all mice were euthanized for dissection.

Tumor volume change curves during treatment indicated that compared to the NS group, tumor growth in the OXA (5 mg of Pt/kg) group showed no significant difference ($P > 0.05$), while the compound **5**−**7** treatment groups (only 2.5 mg of Pt/kg) all exhibited significant inhibition of tumor growth (Figure 8C−H). Tumor weight data depicted in Figure 8I−K revealed that the tumor inhibition rates for compound **5**, **6**, and **7** treatment groups were approximately 60.4, 47.4, and 38.8%, respectively, which were significantly higher than the 37.6% observed in the OXA treatment group. Further observation via hematoxylin and eosin (H&E) staining (Figure 8L) showed that tumor cells in the NS group were densely packed with intact morphology and no obvious damage. The OXA group exhibited only localized death. In contrast, compound **5**−**7** treatment groups displayed extensive areas of tumor necrosis, accompanied by significant nuclear pyknosis. Additionally, Western blot analysis in Figure 8M,N showed that the expression changes of apoptosis-related proteins (Bcl-2, Bax, caspase-3, and cleaved caspase-3) in the tumor tissue were highly consistent with the *in vitro* experimental results (Figure 2D). In summary, compared to OXA, compounds **5**−**7** demonstrate significantly enhanced antitumor activity *in vivo*, underscoring the potential benefits of combining fibrate derivatives with oxaliplatin. Taken together, compounds **5**−**7** demonstrated superior *in vivo* antitumor activity compared with that of OXA, further validating the potential advantages of conjugating fibrates to OXA for enhancing antitumor efficacy.

2.7. Biological Safety Evaluation. Given the obvious toxicity of OXA, we conducted a systematic evaluation of the biosafety profiles of compounds **5**−**7** through comprehensive *in vitro* and *in vivo* experiments. Hemolysis tests showed that after 4 h of incubation, compounds **2**−**7** exhibited good blood compatibility across the concentration range of 15.63 to 500 μM, with hemolysis rates below 5% (Figure 9A−C and Figure S51). Based on the observation that compounds **5**−**7** demonstrated superior efficacy compared to OXA at low doses in previous *in vivo* antitumor studies, we further evaluated their acute toxicity. KM mice were randomly divided into 8 groups ($n = 5$): NS, an OXA group (5 mg of Pt/kg), low-dose compound **5**−**7** groups (2.5 mg of Pt/kg), and high-dose groups (10 mg of Pt/kg). As shown in Figures 9D,E, there was a rapid and significant body weight loss in the OXA group by the fourth day, culminating in a 100% mortality rate on the 12th day. In contrast, the body weight of mice treated with compound **5**−**7** continued to increase throughout the observation period, and all mice in the low-dose compound groups survived (100% survival rate). The overall survival rate in the high-dose groups exceeded 30%, with the compound **7** group showing a survival rate greater than 80%, which was markedly higher than that of the OXA group. These findings indicate that compounds **5**−**7** possess a safety margin significantly wider than that of the safety of OXA within the effective dose range. Monitoring liver and kidney function is essential for drug safety evaluation. We analyzed serum biochemical parameters, including blood urea nitrogen (BUN), uric acid (UA), creatinine (CR), aspartate aminotransferase (AST), and alanine aminotransferase (ALT). As shown in Figure 9F,G, all measured parameters in the compound **5**−**7** treatment groups remained within the normal reference ranges and showed no statistically significant differences compared with the NS group. Furthermore, histopathological examination of major organs (heart, liver, spleen, lungs, and kidneys) via H&E staining (Figure 9H) revealed no significant tissue damage in the compound-treated groups. Although no apparent abnormalities in liver or kidney function were observed in the OXA group, the pronounced weight loss and high mortality rate suggest the presence of substantial toxic effects. We hypothesize that these effects may be primarily attributed to two mechanisms: Pt-based agents such as OXA at doses of 4−6 mg Pt/kg are known to induce chemotherapy-induced peripheral neuropathy (CIPN), which manifests as pain, sensory disturbances, and reduced mobility, thereby significantly impairing animal well-being.[64] Additionally, OXA may lead to anorexia, metabolic dysregulation, and increased energy expenditure, contributing to a rapid weight loss. Accumulating evidence suggests that mediators secreted by the tumor microenvironment play a pivotal role in cancer-related pain.[65] Transient receptor potential vanilloid 1 (TRPV1) channel is implicated in the modulation of pain signaling, inflammatory responses, and tumor progression.[66] Moreover, prolonged OXA treatment has been shown to promote inflammation and upregulate cyclooxygenase-2 (COX-2) expression along with its metabolite prostaglandin E2.[67] COX-2 is regarded as an important target for alleviating neuropathic pain.[68] Consistent with the observed OXA-induced toxicity in this study, immunohistochemical analysis (Figure 9I) demonstrated that OXA treatment significantly increased the expression levels of both TRPV1 and COX-2 in tumor tissues. In conclusion, compounds **5**−**7** exhibit markedly improved biosafety profiles compared with those of OXA. These favorable safety characteristics provide a solid foundation for their further development as next-generation platinum-based anticancer agents.

3. CONCLUSIONS

In conclusion, this study successfully addressed the limitations of the use of OXA in inducing ICD and overcoming immunosuppressive TME through the development of a novel class of fibrate-oxaliplatin(IV) conjugates. These well-designed prodrugs, exemplified by the high-efficiency compound **5** (with an IC_{50} value 319 times lower than that of OXA), demonstrated superior tumor cell accumulation and effectively intracellular release of two active components. The key point is that the fibrate component coordinates multiple attacks: it synergizes with OXA-induced DNA damage, triggers mitochondrial dysfunction and profound endoplasmic reticulum stress, and ultimately leads to intense apoptosis. This

https://doi.org/10.1021/acs.jmedchem.5c02436
J. Med. Chem. 2025, 68, 26328−26347

process integrates with fibrate's unique cholesterol metabolism regulatory function, establishing a "self-amplification" vicious cycle that significantly enhances the release of DAMPs and thereby synergistically amplifies the ICD effect, which is far greater than that of OXA alone. In addition to direct cytotoxicity and enhanced ICD, these conjugates also actively remodel the TME by promoting $CD8^+$ T cell infiltration, inhibiting PD-L1 expression, attenuating Tregs-mediated immunosuppression, and enhancing the secretion of effector molecules such as IFN-γ, TNF-α, and IL-2. Notably, *in vivo* studies have confirmed its powerful antitumor efficacy, along with good biocompatibility and reduced off-target toxicity. This innovative strategy, which integrates metabolic regulation (cholesterol/fibrate) with single-molecule Pt-based chemotherapy, offers a highly promising approach to overcoming tumor immune evasion and provides significant potential for the development of chemoimmunotherapy regimens targeting solid tumors.

4. EXPERIMENTAL SECTION

4.1. Materials and Instrumentations. OXA was purchased from Shandong Platinum Source Pharmaceutical Co., Ltd. CA, FA, CB, GSH, AsA, TEA, TBTU, paraformaldehyde, anhydrous DMSO, and DMF were obtained from Adamas-beta. DMEM medium was purchased from Wisent. Fetal bovine serum (FBS) was acquired from Kangyuan Biotechnology Co., Ltd. Trypsin was obtained from Gibco. MTT was purchased from Macklin. Ethidium bromide (EB), DAPI, the BCA protein assay kit, the SDS-PAGE gel preparation kit, PI, and RNase A were purchased from Solarbio. The genomic DNA extraction kit was obtained from Takara. ^{1}H and ^{13}C NMR measurements were implemented on a spectrometer at 600 MHz (Bruker, AVIII60). Pt content was detected by ICP-MS (Agilent, MS8900). HPLC profiles were obtained using an LC3000I system (Beijing Innovation Tongheng Technology Co., Ltd.). Immunofluorescence was captured by a laser confocal microscope (Zeiss LSM 900).

4.2. Synthesis of Compound 1. OXA (745 mg, 1.73 mmol) and H_2O_2 (30% *w*/*v*, 6 mL) were mixed in a round-bottomed flask and reacted at 70 °C for 7 h. The reaction solution was subsequently cooled overnight at 4 °C to form a white precipitate. The precipitate was washed with water, anhydrous ethanol, and ether and then dried. Yield: 80% (600 mg, 1.39 mmol).

FTMS (*m*/*z*): calcd for $C_8H_{16}N_2O_6Pt$ $(M + Na)^+$, 454.0548; found: 454.0550. IR: 3525.87 (m, ν_{Pt-OH}); 3402.43 (m), 3172.90 (m), 3068.74 (br), 2970.37 (br) (ν_{N-H}); 2947.23 (m) (ν_{C-H}); 2860.43 (m); 1735.93 (s), 1668.42 (s) ($\nu_{C=O}$); 1618.27 (m); 1564.26 (m); 1448.54 (m); 1382.96 (s); 1224.79 (s); 1064.70 (m); 806.24 (s), 763.81 (γ_{C-H}).

4.3. Synthesis of Compound 2. CA (96.6 mg, 0.45 mmol), TEA (51 μL, 0.36 mmol), NHS (77.69 mg, 0.6 mmol), and DCC (102.12 mg, 0.495 mmol) were dissolved in dry acetonitrile (5 mL). The reaction solution was stirred at room temperature for 24 h in a covered flask. The precipitated byproduct, dicyclohexylurea (DCU), was removed either by vacuum filtration or syringe filtration. The filtrate was collected and concentrated to dryness under reduced pressure. The NHS ester was used directly without further purification.

Next, compound **1** (43.20 mg, 0.10 mmol) was reacted with NHS ester (40 mg, 0.128 mmol) in DMSO (3 mL) at 40 °C under a nitrogen atmosphere for 72 h, yielding a clear solution. The solvent was removed under reduced pressure, and ice-cold water was added to obtain a white precipitate. The crude product was purified by silica gel column chromatography (DCM/methanol, *v*/*v*, 20:1) to afford a yellow solid. Yield: 39.00% (24.4 mg, 0.039 mmol). Purity (HPLC): 98.80%.

^{1}H NMR (600 MHz, DMSO-d_6) δ (ppm) = 8.27−8.23 (dd, J = 12,6 Hz,1H), 8.14 (s, 1H), 7.92 (s, 1H), 7.18 (t, J = 4.4 Hz, 3H), 6.76 (d, J = 4.4 Hz, 2H), 2.55−2.53 (m, 1H), 2.33−2.29 (m, 1H), 2.10−2.02 (m, 2H), 1.54−1.49 (m, 2H), 1.49 (s 6H), 1.29−1.08 (m, 4H). ^{13}C NMR (151 MHz, DMSO-*d6*) δ (ppm) = 181.87, 164.11, 164.07, 154.94, 129.23, 124.99, 120.06, 80.74, 62.48, 60.40, 31.28, 26.06, 26.04, 24.06. FTMS (*m*/*z*): calcd $C_{18}H_{25}ClN_2O_8Pt$ $(M + Na)^+$, 650.0947; found, 650.0840. Elemental analysis (%): calcd for $C_{18}H_{25}ClN_2O_8Pt$: C, 34.43; H, 4.01; N, 4.46. Found: C, 34.52; H, 4.18; N, 4.49.

4.4. Synthesis of Compound 3. FA (63.76 mg, 0.20 mmol), TBTU (77.06 mg, 0.24 mmol), and TEA (34 μL, 0.24 mmol) were dissolved in dry DMSO (2 mL), and 15 min later, compound **1** (86.26 mg, 0.20 mmol) was added into the portions. The mixture was stirred at 40 °C under nitrogen for 24 h to form a clear solution. Next, the solvent was removed under reduced pressure, and ice-cold water was added to obtain a white precipitate. The crude product was purified by silica gel column chromatography (DCM/methanol, *v*/*v*, 12:1) to afford a white solid. Yield: 34.00% (49.80 mg, 0.068 mmol). Purity (HPLC): 95.59%.

^{1}H NMR (600 MHz, DMSO-d_6) δ (ppm) 8.16 (d, J = 24 Hz, 1H), 7.95 (s, 1H), 7.79 (d, J = 12 Hz, 2H), 7.60 (t, J = 8.7 Hz, 4H), 7.17 (t, J = 10.2 Hz, 1H), 6.81 (d, J = 5.9 Hz, 2H), 2.54 (d, J = 11.4 Hz, 1H), 2.31 (d, J = 6 Hz, 1H), 2.11−1.98 (dd, J = 42 Hz, 2H), 1.48(s, 6H), 1.49−1.46 (m, 2H), 1.30−1.09 (m, 4H). ^{13}C NMR (151 MHz, DMSO-d_6) δ (ppm) = 193.27, 180.98, 163.62, 159.74, 136.87, 136.40, 131.78, 131.38, 128.67, 128.51, 116.56, 80.39, 62.06, 30.84, 25.76, 25.44, 23.63. FTMS (*m*/*z*): calcd $C_{25}H_{29}ClN_2O_9Pt$ $(M + H)^+$, 732.0460; found, 732.1284. Elemental analysis (%): calcd for $C_{25}H_{29}ClN_2O_9Pt$: C, 41.02; H, 3.99; N, 3.83. Found: C, 41.08; H, 3.94; N, 3.89.

4.5. Synthesis of Compound 4. CB (57.83 mg, 0.20 mmol), TBTU (77.06 mg, 0.24 mmol), and TEA (34 μL, 0.24 mmol) were dissolved in dry DMSO (2 mL), and 15 min later, compound **1** (86.26 mg, 0.20 mmol) was added into the portions. The mixture was stirred at 40 °C under nitrogen for 48 h to form a clear solution. Next, the solvent was removed under reduced pressure and ice-cold water was added to obtain a white precipitate. The crude product was purified by silica gel column chromatography (DCM/methanol, *v*/*v*, 12:1) to afford a white solid. Yield: 24.50% (34.60 mg, 0.049 mmol). Purity (HPLC): 96.40%.

^{1}H NMR (600 MHz, DMSO-d_6) δ (ppm) = 8.38−8.28 (m, 1H), 8.17 (s, 1H), 7.92 (s, 1H), 7.18 (s, 1H), 7.09 (d, J = 8.9 Hz, 2H), 6.76−6.70 (m, 2H), 3.01−2.95 (m, 1H), 2.70 (s, 1H), 2.37 (d, J = 19.8 Hz, 1H), 2.09 (s, 2H), 2.01 (d, J = 16.3 Hz, 2H), 1.49 (s, 2H), 1.43 (s, 6H), 1.27−0.98 (m, 4H). ^{13}C NMR (151 MHz, DMSO-d_6) δ (ppm) = 181.11, 163.05, 154.41, 128.80, 125.95, 116.84, 79.14, 61.44, 59.29, 33.31, 30.26, 25.25, 25.11, 24.90, 24.18, 23.04. FTMS (*m*/*z*): calcd $C_{21}H_{28}Cl_2N_2O_8Pt$ $(M + Na)^+$, 724.0870; found, 724.0773. Elemental analysis (%): calcd for $C_{21}H_{28}Cl_2N_2O_8Pt$: C, 35.91; H, 4.02; N, 3.99. Found: C, 35.98; H, 4.08; N, 3.94.

4.6. Synthesis of Compound 5. CA (137 mg, 0.64 mmol), TBTU (77.06 mg, 0.24 mmol), and TEA (102 μL, 0.72 mmol) were dissolved in dry DMF (2 mL), and 15 min later, compound **1** (86.26 mg, 0.20 mmol) was added into the portions. The mixture was stirred at 40 °C under nitrogen for 48 h to form a clear solution. Then, the solvent was removed under reduced pressure and ice-cold water was added to obtain a white precipitate. The crude product was purified by silica gel column chromatography (DCM/methanol, *v*/*v*, 60:1) to afford a white solid. Yield: 49% (80.40 mg, 0.098 mmol). Purity (HPLC): 98.06%.

^{1}H NMR (600 MHz, DMSO-d_6) δ (ppm) = 8.43 (d, J = 9.1 Hz, 2H), 8.08 (d, J = 12, 2H), 7.20 (d, J = 9.1 Hz, 4H), 6.76 (d, J = 9.1 Hz, 4H), 2.13−2.11 (t, 2H), 1.52 (d, J = 9.6 Hz, 2H), 1.46 (s, 12H), 1.40 (d, J = 9.4 Hz, 2H), 1.10−1.05 (m, 4H). ^{13}C NMR (151 MHz, DMSO-d_6) δ (ppm): 180.85, 163.38, 154.67, 129.35, 125.38, 120.24, 80.16, 62.13, 31.49, 26.19, 25.86, 23.99. FTMS (*m*/*z*): calcd $C_{28}H_{34}Cl_2N_2O_{10}Pt$ $(M + Na)^+$, 846.1238; found, 846.1140. Elemental analysis (%): calcd for $C_{28}H_{34}Cl_2N_2O_{10}Pt$: C, 40.79; H, 4.16; N, 3.40. Found: C, 40.72; H, 4.18; N, 3.49.

4.7. Synthesis of Compound 6. FA (191.25 mg, 0.6 mmol), TBTU (77.06 mg, 0.24 mmol), and TEA (102 μL, 0.72 mmol) were

https://doi.org/10.1021/acs.jmedchem.5c02436
J. Med. Chem. 2025, 68, 26328−26347

dissolved in dry DMF (2 mL), and 15 min later, compound **1** (86.26 mg, 0.20 mmol) was added into the portions. The mixture was stirred at 40 °C under nitrogen for 48 h to form a clear solution. Then, the solvent was removed under reduced pressure and ice-cold water was added to obtain a white precipitate. The crude product was purified by silica gel column chromatography (DCM/methanol, *v*/*v*, 80:1) as eluent to afford a white solid. Yield: 34% (69.80 mg, 0.068 mmol). Purity (HPLC): 98.45%.

^{1}H NMR (600 MHz, DMSO) δ (ppm) = 8.44 (s, 2H), 8.06 (s, 2H), 7.78 (d, J = 8.4 Hz, 4H), 7.62 (d, J = 8.8 Hz, 4H), 7.57 (d, J = 8.4 Hz, 4H), 6.81 (d, J = 6.8 Hz, 4H), 2.34 (s, 2H), 2.12 (d, J = 12.3 Hz, 2H), 1.56 (d, J = 8.8 Hz, 12H), 1.47 (d, J = 8.5 Hz, 2H), 1.41 (d, J = 12.1 Hz, 2H), 1.06−1.00 (m, 2H). ^{13}C NMR (151 MHz, DMSO-d_6) δ (ppm): 193.17, 180.01, 162.71, 159.36, 136.90, 136.27, 131.80, 131.27, 128.93, 128.46, 116.57, 79.73, 61.68, 31.00, 25.65, 25.48, 23.48. FTMS (*m*/*z*): calcd $C_{42}H_{42}Cl_2N_2O_{12}Pt$ $(M + H)^+$, 1032.7840; found, 1032.1839. Elemental analysis (%): calcd for $C_{42}H_{42}Cl_2N_2O_{12}Pt$: C, 48.84; H, 4.10; N, 2.71. Found: C, 48.89; H, 4.18; N, 2.75.

4.8. Synthesis of Compound 7. CB (185.05 mg, 0.64 mmol), TBTU (77.06 mg, 0.24 mmol), and TEA (102 μL, 0.72 mmol) were dissolved in dry DMF (2 mL), and 15 min later, compound **1** (86.26 mg, 0.20 mmol) was added into the portions. The mixture was stirred at 40 °C under nitrogen for 48 h to form a clear solution. Then, the solvent was removed under reduced pressure and ice-cold water was added to obtain a white precipitate. The crude mixture was purified by silica gel column chromatography (DCM/methanol, *v*/*v*, 60:1) to afford a white solid. Yield: 25.00% (52.60 mg, 0.05 mmol). Purity (HPLC): 99.64%.

^{1}H NMR (600 MHz, DMSO-d_6) δ (ppm) = 8.44 (d, J = 6.4 Hz, 2H), 8.13 (d, J = 9.1 Hz, 2H), 7.11 (d, J = 8.7 Hz, 4H), 6.74 (d, J = 8.9 Hz, 4H), 3.05−2.92 (m, 2H), 2.42−2.35 (m, 2H), 2.07−1.97 (m, 4H), 1.53−1.50 (m, 2H), 1.46 (d, J = 4.2 Hz, 12H), 1.11−1.02 (m, 2H). ^{13}C NMR (151 MHz, DMSO-d_6) δ (ppm) = 180.16, 180.11, 162.30, 154.11, 128.89, 126.35, 117.02, 78.62, 78.59, 61.32, 61.11, 61.08, 61.04, 39.46, 33.29, 30.46, 25.40, 25.26, 24.91, 24.74, 24.21, 22.96. FTMS (*m*/*z*): calcd $C_{34}H_{40}Cl_4N_2O_{10}Pt$ $(M + Na)^+$, 994.1085; found, 994.0983. Elemental analysis (%): calcd for $C_{34}H_{40}Cl_4N_2O_{10}Pt$: C, 41.95; H, 4.14; N, 2.88. Found: C, 41.87; H, 4.17; N, 2.93.

4.9. Cyclic Voltammetry Test. The reduction potential of the platinum(IV) compound was measured using a three-electrode system (CHI760e), comprising a glassy carbon electrode as the working electrode, a saturated calomel electrode as the reference electrode, and a platinum sheet electrode as the counter electrode. The scan rate was set at 100 mV/s. All electrochemical measurements were conducted in PBS buffer containing 0.1 mM platinum(IV) compound and 0.1 M KCl.

4.10. Log $P_{o/w}$ Determination. The Log P values were determined by using the shake-flask method. Standard regression equations for the concentration−absorbance (C−A) relationship of the two-phase system were established by UV spectrophotometry. The compounds were dissolved in water-saturated *n*-octanol and equilibrated with octanol-saturated water after 24 h of shaking in the dark. The concentrations of the compounds in each phase were quantified to calculate the Log $P_{o/w}$ values. All measurements were performed in triplicate.

4.11. Stability of Compounds in PBS and Plasma. Compounds **2**−**4** were dissolved in a PBS/DMF buffer (9:1, *v*/*v*), while **5**−**7** were dissolved in PBS/DMF (3:2, *v*/*v*). All solutions were incubated at 37 °C in the dark. The stability of each compound was monitored at 0, 12, 24, and 72 h using an HPLCONE-5 C18A column (250 × 10 mm, 5 μm). The mobile phase for compound **2** consisted of methanol/water (20:80, *v*/*v*, containing 0.1% formic acid). The mobile phase of compounds **3**−**7** was analyzed using methanol/water (60:40, *v*/*v*, containing 0.1% formic acid). The UV detector was set at a wavelength of 254 nm.

In vivo stability: Compounds **5**−**7** were mixed with plasma and incubated in the dark at 37 °C. Samples were taken at time points of 0, 24, 48, and 72 h, respectively, and detected by HPLC. The detection conditions and methods were consistent with the above *in vitro* stability.

4.12. Reduction Kinetics. Compounds **2**−**4** (1 mM) were dissolved in PBS/DMF (9:1, *v*/*v*) containing AsA (10 mM) or GSH (10 mM), respectively. Compounds **5**−**7** (1 mM) were dissolved in PBS/DMF (3:2, *v*/*v*) containing AsA (10 mM) or GSH (10 mM), respectively. All solutions were incubated at 37 °C in the dark. The release profile of each compound was determined by HPLC. The mobile phase was the same as the conditions in stability study.

4.13. Cell Culture. The human breast cancer cell line (MCF-7), human ovarian cancer cell line (A2780), mouse breast cancer cell line (4T1), human renal cortex proximal tubule epithelial cell line (HK2), and human umbilical vein endothelial cells (HUVECs) were obtained from Pricella and Shanghai Fuheng Biotechnology Co., Ltd. Cells were all cultured in DMEM containing 10% FBS at 37 °C, 5% CO_2, and 90% humidity. The short-term OXA-resistant MCF-7/OXA cell line was established through gradual exposure to increasing concentrations of OXA. Following stable proliferation under culture conditions containing 5 μM oxaliplatin, cell viability was assessed using the MTT assay.

4.14. Antiproliferative Activity. The viability of cells exposed to these compounds was evaluated by the MTT colorimetric method. Briefly, cells were seeded into 96-well plates at a density of 3000 cells/well and allowed to attach overnight. Then, compounds were administered into each well via a double and half dilution method, and the first hole was 100 μM. After continuing exposure for 24 or 72 h, the cells were incubated with MTT (10 μL and 5 μg/μL in PBS) for 4 h. The MTT containing culture medium was removed carefully, and DMSO (100 μL) was added to each well to dissolve the formazan. The absorbance at 570 nm was tested with a microplate reader (BioTek).

4.15. Intracellular Release. Cells were seeded in 6-well plates and incubated for 24 h to allow attachment. Then, the original culture medium was discarded and replaced with fresh medium containing the test compounds (100 μM), respectively. 3 h later, the cells were harvested and centrifuged to remove the supernatant. Subsequently, the cells were resuspended in 1 mL of organic solvent (methanol/dichloromethane, 1:1, *v*/*v*), and the supernatant was collected following high-speed centrifugation. The extracted samples were dried under a vacuum, and the drug content was quantified using HPLC. The HPLC analytical conditions were maintained in accordance with those used for the previously described purity analysis.

4.16. Hoechst 33342 Staining. After the cells were exposed to compounds (5 μM) for 24 h, the culture medium was removed, and the cells were stained with Hoechst 33342 (1 μg/mL) at 37 °C in the dark for 15 min. Subsequently, the cells were rinsed with PBS, and the fluorescence images were captured using a fluorescence microscope (Nikon).

4.17. Detection of Intracellular ROS. Intracellular ROS levels were assessed using the ROS fluorescence probe 2′,7′- dichlorofluorescein diacetate (DCFH-DA) (Invitrogen). MCF-7 cells were plated in 6-well plates and allowed to adhere overnight. The cells were then treated with compounds (5 μM) for 24 h. Following treatment, the cells were washed twice with PBS and incubated with DCFH-DA at 37 °C for 20 min in the dark. After an additional wash with PBS, the pictures were obtained using fluorescence microscopy (Nikon).

4.18. Mitochondrial Membrane Potential. MCF-7 cells cultured in 6-well plates were treated with compounds (5 μM) for 24 h. After treatment, the cells were washed with PBS and incubated with JC-1 dye working buffer at 37 °C for 20 min in the dark. Following a wash with JC-1 buffer, images were captured using fluorescence microscopy (Nikon).

4.19. ICP-MS Detection. Following treatment with compounds (10 μM) for 8 h at 37 °C, cells were harvested, washed, and counted. Genomic DNA was extracted from separately treated cells, and its concentration was determined by a visible spectrophotometer (Quawell Q5000). All samples were lyophilized and digested with nitric acid (HNO_3, 65%, suprapure grade). Pt content was quantified by ICP-MS.

https://doi.org/10.1021/acs.jmedchem.5c02436
J. Med. Chem. 2025, 68, 26328−26347

4.20. Comet Assay. To evaluate DNA damage induced by Pt-based compounds, a comet assay was performed. MCF-7 cells were seeded into 12-well plates and exposed to various treatments for 24 h. Then, cells were collected, resuspended in low-melting-point agarose (1%), and spread onto the glass slides precoated with 0.8% normal agarose. After solidification at 4 °C, the slides were immersed into 50 mL of alkaline lysis buffer (containing 1% Triton X-100 and 10% DMSO) for 24 h at 4 °C. The slides were then transferred to electrophoresis buffer for 40 min and subjected to electrophoresis at 300 mA for 30 min. Finally, the slides were stained with an EB solution (10 mg/mL) for 5 min, and the fluorescence pictures were obtained via a fluorescence microscope (Nikon). The images were analyzed using the comet assay software project (CASP) image analysis program, and the "olive tail moment" (OTM) was calculated as an indicator of DNA damage.

4.21. Cell Cycle Analysis. Following 24 h of compound treatment (2.5 μM), cells were harvested, washed twice with cold PBS, and fixed with cold 75% ethanol at −20 °C for 48 h. After fixation, the cells were centrifuged, the supernatant was removed, and the pellet was resuspended in 500 μL of PBS. RNase (2.5 μL, 10 mg/mL) was added, and the mixture was incubated at 37 °C for 30 min. Finally, PI dyeing solution was added, and the samples were incubated for an additional 30 min in the dark. The DNA content of the cells was analyzed by using flow cytometry (CytoFLEX).

4.22. Annexin V-FITC/PI Staining. Cells were treated with the tested compounds (2.5 μM) for 36 h and then digested with no-EDTA trypsin. Following two washes with PBS, the cells were resuspended in 500 μL of the binding buffer. Next, 5 μL of Annexin V-FITC staining solution (20 min incubation) and 5 μL of PI solution (15 min incubation) were added in the dark, respectively. The proportion of apoptotic cells was detected by flow cytometry (CytoFLEX).

4.23. Dil Staining. MCF-7 cells cultured on glass culture dishes were treated with various compounds (5 μM) for 12 h. After treatment, the cells were washed twice with PBS and fixed with 4% paraformaldehyde for 30 min. The cells were then incubated with Dil staining solution (10 μM) at 37 °C for 30 min. After thorough washing, a DAPI staining solution was applied to label the nuclei. The final image was captured by using a confocal laser microscope (Zeiss LSM900).

4.24. Acute Toxicity Assessment. Forty 4-week-old Kunming mice were randomly divided into eight groups (n = 5). The mice were purchased from SPF (Beijing) Biotechnology Co., Ltd. NS (100 μL), OXA (5 mg of Pt/kg), and compounds **5**−**7** (2.5 mg of Pt/kg and 10 mg of Pt/kg, respectively) were administered intravenously every 2 days for a total of 14 days, respectively. Body weight changes were recorded throughout the experiment, and the survival rate of the mice was calculated at the end of the observation period.

4.25. Antitumor Activity in Mouse Model. 4-week-old Balb/c mice were purchased from SPF (Beijing) Biotechnology Co., Ltd. and housed a week. Then, 4T1 cells (1×10^6 cells per mouse) were injected into the right oxter of the mice. After tumor establishment, the tumor-bearing mice were randomly assigned to five groups (n = 6): (i) NS, (ii) OXA (5 mg-Pt/kg), (iii) compound **5** (2.5 mg-Pt/kg), (iv) **6** (2.5 mg-Pt/kg), and (v) 7 (2.5 mg-Pt/kg). Body weight and tumor volume of each mouse were recorded every 2 days. Tumor volume (V) was calculated using the formula: $V = W^2 \times L/2$, where W represents tumor width, and L represents tumor length.

All animal experiments in this work were conducted in accordance with the Regulations on the Administration of Laboratory Animals and relevant national laws and regulations, following a protocol approved by the Animal Care and Use Committee of Hebei University. Hebei University Affidavit of Approval of Animal Welfare and Ethics, approval number IACUC-2021XS043.

4.26. Western Blot Analysis. Cells were seeded into 6-well plates and exposed to various compounds for 24 h. Following treatment, cells were lysed in RIPA buffer supplemented with 1% phenylmethylsulfonyl fluoride (PMSF) for 40 min on ice. Protein concentrations were determined using a BCA protein assay kit. For tumor tissue samples, approximately 50 mg of tissue was homogenized in RIPA buffer containing 1% PMSF by using a tissue homogenizer. The lysates were centrifuged at high speed to collect the supernatant, and protein concentrations were measured using the BCA method. Equal amounts of protein were separated by SDS-PAGE gel and transferred onto a 0.45 μm poly(vinylidene fluoride) (PVDF) membrane. The membrane was blocked with 5% skim milk in TBST at room temperature for 3 h. After full washing with TBST, the membrane was incubated with primary antibodies diluted in TBST at 4 °C overnight. Following four washes with TBST, the membrane was incubated with the corresponding secondary antibody for 90 min at room temperature. Protein bands were developed by ECL (Thermo, model 34095) and captured by a chemiluminescence imaging analysis system, and band intensities were quantified using ImageJ software. The primary antibodies and their dilutions were as follows: Bax (60267-1-Ig, 1:10000, Proteintech), Bcl-2 (60178-1-Ig, 1:5000, Proteintech), PPARα (668261-Ig, 1:5000, Proteintech), Caspase-3 (66470-1-Ig, 1:3000, Proteintech), CD8 (RM3357, 1:1000, Biodragon), Foxp3 (RM4985, 1:1000, Biodragon), GAPDH (60004-1-Ig, 1:3000, Proteintech), β-actin (66009-1-Ig, 1:5000, Proteintech), COX-2 (66351-1-Ig, 1:3000, Proteintech), and TRPV1 (66983-1-Ig, 1:4000, Proteintech).

4.27. Immunofluorescence. Cells were seeded into confocal microdishes and treated with various compounds (5 μM) for 24 h. Then, the cells were washed, fixed with 4% paraformaldehyde for 30 min, permeabilized with 0.5% Triton X-100, and subsequently blocked with 5% BSA solution for 2 h. Next, the cells were incubated overnight at 4 °C with the primary antibody GRP78 (11587-1-Ig, 1:500, Proteintech) and CHOP (15204-1-AP, 1:500, Proteintech). After washing with PBS containing 5% BSA, the cells were incubated with Alexa Fluor 488/594-conjugated goat antirabbit IgG (H + L) secondary antibody for another 1 h. Before being captured by a laser confocal microscope, DAPI was added to label the cell nuclei.

4.28. ATP Release Assay. MCF-7 cells were seeded into 96-well plates at a density of 4×10^3 cells per well and cultured for 24 h. Subsequently, cells were treated with various compounds (5 μM) for 24 h. The culture medium was then collected, and the ATP concentration was quantified using an ATP assay kit (Beyotime, S0026) according to the manufacturer's instructions.

4.29. Detection of ICD *In Vitro*. MCF-7 cells were inoculated in plates with 1.2×10^5 cells per well. After adhesion, the cells were treated with PBS, OXA, and compound **5**−**7** (5 μM) for 24 h, respectively. The collected cells were then washed three times with PBS, fixed with 4% paraformaldehyde, and washed again three times with PBS. The cells were blocked with 0.5% BSA for 1 h and incubated overnight at 4 °C with CRT primary antibody (10292-1-AP, 1:500 Proteintech) diluted in 0.5% BSA. After three additional washes with 0.5% BSA, the cells were incubated with Alexa Fluor 594-conjugated goat antirabbit IgG (H + L) secondary antibody for 1 h. Finally, before capturing fluorescence images by a microscope (Zeiss LSM 900), the cell nucleus was mounted with DAPI.

4.30. Immunofluorescence. Tumor tissues were embedded in paraffin and sectioned. The paraffin sections were deparaffinized, rehydrated, and subjected to antigen retrieval. Subsequently, the sections were washed three times with PBS and blocked with 5% BSA or normal serum for 30 min. The sections were then incubated overnight at 4 °C with primary antibodies against CRT and HMGB1. After washing with PBS, fluorescently labeled secondary antibody (Alexa Fluor 488) was applied, and the sections were incubated in the dark for 1 h. Following another wash with PBS, DAPI was added for nuclear staining. Confocal microscopy was used to capture multi-channel fluorescence images, which were analyzed using ZEN software.

4.31. Immunohistochemistry. After dewaxing the paraffin sections to water, antigen retrieval was carried out, and they were washed with PBS three times. Then, 3% hydrogen peroxide was used to block endogenous peroxidase for 25 min, and PBS was used for washing three times. Then, 3%BSA was blocked for 30 min, and CD8 or PD-L1 primary antibodies were added overnight at 4 °C. The next day, wash with PBS, add HRP-labeled secondary antibody, and incubate at room temperature for 50 min. After PBS washing, DAB

https://doi.org/10.1021/acs.jmedchem.5c02436
J. Med. Chem. 2025, 68, 26328−26347

color development (controlled under the microscope) and hematoxylin counterstain the nucleus. Finally, the film was sealed and observed under a white light microscope.

4.32. Detection of Cytokine. Serum samples were collected from BALB/c mice in the tumor suppression experiment. The concentration of IFN-γ, TNF-α, and IL-2 was measured using IFN-γ ELISA kit (Beyotime, PI508), TNF-α ELISA kit (Solabao, SEKM-0034), and IL-2 ELISA kit (Solabao, SEKM-0004) in accordance with the manufacturer's protocol.

4.33. Cholesterol Content of Tumor Tissue and Blood. Fresh tumor tissues treated with various drugs were rinsed with normal saline, sectioned into small fragments, and homogenized using a tissue grinder. The homogenates were centrifuged at 2000 rpm for 10 min, and the supernatant was collected for further analysis. Total cholesterol levels were quantified using a commercial assay kit (total cholesterol assay kit, Nanjing Jiancheng Institute of Bioengineering, Cat. No. A111-1) in accordance with the manufacturer's instructions. Blood samples from BALB/c mice used in tumor suppression experiments were similarly collected and analyzed by following the same protocol.

4.34. Hemolysis Test *In Vitro*. PBS solutions containing various concentrations of the test compounds (500 μM, 250 μM, 125 μM, 62.5 μM, 31.25 μM, and 15.625 μM) were mixed with an equal volume of 2% erythrocyte suspension. H_2O and PBS were used as positive and negative controls, respectively. After 4 h of incubation at 37 °C, the mixtures were centrifuged at 3000 rpm for 15 min, and the supernatants were collected. The absorbance was measured at 540 nm by using a microplate reader. The hemolysis rate was calculated using the following formula:

$$\text{Hemolysis rate } (\%) = \frac{\text{OD}(i) - \text{OD}(\text{PBS})}{\text{OD}(\text{H}_2\text{O}) - \text{OD}(\text{PBS})} \times 100\%$$

4.35. Flow Cytometry Analysis of T cells and DCs. Fresh tumor tissues from mice were rinsed with normal saline, minced into small fragments, and transferred to tissue digestion solution (RPMI-1640 medium supplemented with 2 mg/mL collagenase IV, 1 mg/mL DNase I, and 2% FBS) for enzymatic digestion at 37 °C with agitation at 200 rpm for 1 h. The digested tissue was filtered through a 70 μm cell strainer to obtain a single-cell suspension. The cells were centrifuged, collected, and resuspended in 2 mL of red blood cell lysis buffer and incubated at 4 °C for 10 min. Finally, the cells were washed twice with PBS and processed for staining. For T cell characterization, cells were stained with antimouse CD3-PE (PE-FcA65659, Proteintech), antimouse CD4-APC (APC-65662, Proteintech), and antimouse CD8-FITC (FITC-98472−2, Proteintech). For DC analysis, cells were stained with antimouse CD11c-FITC (FITC-65602, Proteintech), antimouse CD80-PE (PE-FcA98158, Proteintech), and antimouse CD86-APC (APC-FcA98025, Proteintech). After 30 min of incubation in the dark, samples were analyzed using a flow cytometer.

4.36. Statistical Analysis. All statistical analyses were performed using GraphPad Prism version 10.0. Data were expressed as mean ± SD. Statistical comparisons were conducted using t ;test. Each experiment was independently repeated at least three times to ensure reproducibility.

■ ASSOCIATED CONTENT

Supporting Information

The Supporting Information is available free of charge at https://pubs.acs.org/doi/10.1021/acs.jmedchem.5c02436.

^{1}H/^{13}C NMR, FTMS, IR, and HPLC spectra of compounds; stability of the compound was determined by high-performance liquid chromatography; Hoechst 33342 staining and quantitative analysis after drug action on MCF-7 cells; cyclic voltammetry of compounds; reducing ability of compounds determined by HPLC; flow cytometry used to detect changes in the cell cycle and apoptosis; JC-I/ROS and quantification of fluorescence intensity after drug action on MCF-7 cells; Dil staining of cells after drug action; hemolytic changes of compounds **2**−**4**; MTT value of drug combination effects (PDF)

Molecular formula strings (CSV)

■ AUTHOR INFORMATION

Corresponding Authors

Longfei Li − *Key Laboratory of Medicinal Chemistry and Molecular Diagnosis of Ministry of Education, Key Laboratory of Pharmaceutical Quality Control of Hebei Province, College of Pharmacy, Hebei University, Baoding, Hebei 071002, P. R. China;* orcid.org/0000-0001-8435-4006; Email: lilongfei@hbu.edu.cn

Xue-Qing Song − *Key Laboratory of Medicinal Chemistry and Molecular Diagnosis of Ministry of Education, Key Laboratory of Pharmaceutical Quality Control of Hebei Province, College of Pharmacy, Hebei University, Baoding, Hebei 071002, P. R. China;* orcid.org/0000-0001-5527-5261; Email: sxqing@hbu.edu.cn

Authors

Xue-Jiao Liang − *Key Laboratory of Medicinal Chemistry and Molecular Diagnosis of Ministry of Education, Key Laboratory of Pharmaceutical Quality Control of Hebei Province, College of Pharmacy, Hebei University, Baoding, Hebei 071002, P. R. China*

Xu Guo − *Key Laboratory of Medicinal Chemistry and Molecular Diagnosis of Ministry of Education, Key Laboratory of Pharmaceutical Quality Control of Hebei Province, College of Pharmacy, Hebei University, Baoding, Hebei 071002, P. R. China*

Peng-Hui Zhu − *Key Laboratory of Medicinal Chemistry and Molecular Diagnosis of Ministry of Education, Key Laboratory of Pharmaceutical Quality Control of Hebei Province, College of Pharmacy, Hebei University, Baoding, Hebei 071002, P. R. China*

Zi-Han Zhao − *Key Laboratory of Medicinal Chemistry and Molecular Diagnosis of Ministry of Education, Key Laboratory of Pharmaceutical Quality Control of Hebei Province, College of Pharmacy, Hebei University, Baoding, Hebei 071002, P. R. China*

Zhihao You − *Key Laboratory of Medicinal Chemistry and Molecular Diagnosis of Ministry of Education, Key Laboratory of Pharmaceutical Quality Control of Hebei Province, College of Pharmacy, Hebei University, Baoding, Hebei 071002, P. R. China;* orcid.org/0000-0002-5741-7806

Kan Yang − *Key Laboratory of Medicinal Chemistry and Molecular Diagnosis of Ministry of Education, Key Laboratory of Pharmaceutical Quality Control of Hebei Province, College of Pharmacy, Hebei University, Baoding, Hebei 071002, P. R. China*

Yali Song − *Key Laboratory of Medicinal Chemistry and Molecular Diagnosis of Ministry of Education, Key Laboratory of Pharmaceutical Quality Control of Hebei Province, College of Pharmacy, Hebei University, Baoding, Hebei 071002, P. R. China;* orcid.org/0000-0002-7011-6741

Complete contact information is available at: https://pubs.acs.org/10.1021/acs.jmedchem.5c02436

Author Contributions

[1]Xue-Jiao Liang and Xu Guo contributed equally.

Notes

The authors declare no competing financial interest.

■ ACKNOWLEDGMENTS

This work was supported by the National Natural Science Foundation of China (22373030 and 82273792), Natural Science Foundation of Hebei Province (B2024201035), Hebei Province Yan Zhao Golden Platform Talent Gathering Plan Backbone Talent Project (Education Platform) (HJYB202523), "IT2023C01" Innovation Team Project of Hebei University (521201623023), and The Excellent Youth Research Innovation Team of Hebei University (QNTD202406). Scheme [1] image support was provided by Figdraw.

■ ABBREVIATIONS

AsA,Ascorbic acid; ABCA1,ATP-binding cassette transporter A1; AST,Aspartate aminotransferase; ALT,Alanine aminotransferase; Bax,Bcl-2 associated X; Bcl-2,B-cell lymphoma 2; BUN,Blood urea nitrogen; CRT,Calreticulin; CA,Clofibric acid; CB,Cyclopentetic acid; CV,Cyclic voltammetry; CR,Creatinine; CHOP,C/EBP-homologous protein; Caspase-3,Cysteine-dependent aspartate-specific protease-3; CIPN,Peripheral neuropathy; COX-2,Cyclooxygenase-2; DAMPs,Damage-associated molecular patterns; DMF,*N*,*N*-Dimethylformamide; DCU,Dicyclohexylurea; DCFH-DA,2′,7′-Dichlorofluorescein; DMAP,4-Dimethylaminopyridine; DMSO,Dimethyl sulfoxide; DC,Dendritic cell; Dil,1,1-Dioctadecyl-3,3,3,3-tetramethylindocarbocyanine perchlorate; ERS,Endoplasmic reticulum stress; EB,Ethidium bromide; FAO,Fatty acid oxidation; FTMS,Fourier transform mass spectrometry; FA,Fenofibric acid; FBS,Fetal bovine serum; GSH,Glutathione; GRP78,Glucose-regulated protein 78; HMGB1,High-mobility group protein B1; HDL,High-density lipoprotein; H2O2,Hydrogen peroxide; HPLC,High-performance liquid chromatography; H&E,Hematoxylin and eosin; IFN-γ,Interferon-γ; ICD,Immunogenic cell death; IR,Infrared spectrum; ICP-MS,Inductively coupled plasma mass spectrometry; IC50 values,Half-maximal inhibitory concentration; MTT,3-(4,5-Dimethylthiazol-2-yl)-2,5-diphenyltetrazolium bromide; NS,Normal saline; NADPH,Nicotinamide adenine dinucleotide phosphate; OXA,Oxaliplatin; PPARα,Peroxisome proliferator-activated receptor α; PBS,Phosphate buffers; PI,Propidium iodide; PMSF,Phenylmethylsulfonyl fluoride; ROS,Reactive oxygen species; RIPA,Ripa lysis buffer; SDS-PAGE,Sodium dodecyl sulfate polyacrylamide gel electrophoresis; Tregs,Regulatory T cells; TME,Tumor microenvironment; TEA,Containing triethylamine; TBTU,2-(1*H*-benzotriazole-1-yl)-1,1,3,3-tetramethyl-uronium tetrafluoroborate; TRPV1,Transient receptor potential vanilloid 1; UA,Uric acid; UV,Ultraviolet/visible spectroscopy; UPR,Unfolded protein response; $\Delta\Psi$m,Mitochondrial transmembrane potential.

■ REFERENCES

(1) Ahmadi, M.; Abbasi, R.; Rezaie, J. Tumor Immune Escape: Extracellular Vesicles Roles and Therapeutics Application. *Cell Commun. Signal.* **2024**, *22*, 9.

(2) Fucikova, J.; Kepp, O.; Kasikova, L.; Petroni, G.; Yamazaki, T.; Liu, P.; Zhao, L.; Spisek, R.; Kroemer, G.; Galluzzi, L. Detection of Immunogenic Cell Death and its Relevance for Cancer Therapy. *Cell Death Dis.* **2020**, *11*, 1013.

(3) Aria, H.; Rezaei, M. Immunogenic Cell Death Inducer Peptides: A New Approach for Cancer Therapy, Current Status and Future Perspectives. *Biomed. Pharmacother.* **2023**, *161*, No. 114503.

(4) Ding, Q.; Tang, W.; Li, X.; Ding, Y.; Chen, X.; Cao, W.; Wang, X.; Mo, W.; Su, Z.; Zhang, Q.; Guo, H. Mitochondrial-targeted Brequinar Liposome Boosted Mitochondrial-related Ferroptosis for Promoting Checkpoint Blockade Immunotherapy in Bladder Cancer. *J. Controlled Release* **2023**, *363*, 221−234.

(5) Lv, J.; Cai, J.; Yuan, K.; Wang, J.; Xu, Y.; Huang, X.; Wang, J.; Dai, Z.; Pan, Y.; Zhao, C.; Liu, J.; Gui, L.; Wu, J.; Zhong, Q.; Yuan, Z.; Zheng, J. Immunogenic Cell Death Inducers: Current Advances and Future Perspectives. *Coordin. Chem. Rev.* **2025**, *542*, No. 216846.

(6) Sen, S.; Won, M.; Levine, M. S.; Noh, Y.; Sedgwick, A. C.; Kim, J. S.; Sessler, J. L.; Arambula, J. F. Metal-based Anticancer Agents as Immunogenic Cell Death Inducers: the Past, Present, and Future. *Chem. Soc. Rev.* **2022**, *51*, 1212−1233.

(7) Li, J.; Zhou, S.; Yu, J.; Cai, W.; Yang, Y.; Kuang, X.; Liu, H.; He, Z.; Wang, Y. Low Dose Shikonin and Anthracyclines Coloaded liposomes Induce Robust Immunogenetic Cell Death for Synergistic Chemo-immunotherapy. *J. Controlled Release* **2021**, *335*, 306−319.

(8) Galluzzi, L.; Guilbaud, E.; Schmidt, D.; Kroemer, G.; Marincola, F. M. Targeting Immunogenic Cell Stress and Death for Cancer Therapy. *Nat. Rev. Drug Discovery* **2024**, *23*, 445−460.

(9) Gu, J.; Zhu, N.; Li, H.; Zhao, T.; Zhang, C.; Liao, D.; Qin, L. Cholesterol Homeostasis and Cancer: A New Perspective on the Low-density Lipoprotein Receptor. *Cell. Oncol.* **2022**, *45*, 709−728.

(10) Xiao, M.; Xu, J.; Wang, W.; Zhang, B.; Liu, J.; Li, J.; Xu, H.; Zhao, Y.; Yu, X.; Shi, S. Functional Significance of Cholesterol Metabolism in Cancer: from Threat to Treatment. *Exp. Mol. Med.* **2023**, *55*, 1982−1995.

(11) Jin, J.; Zhao, Q.; Wei, Z.; Chen, K.; Su, Y.; Hu, X.; Peng, X. Glycolysis-cholesterol Metabolic Axis in Immuno-oncology Microenvironment: Emerging Role in Immune Cells and Immunosuppressive Signaling. *Cell Biosci.* **2023**, *13*, 189.

(12) Zheng, M.; Zhang, W.; Chen, Y.; Guo, H.; Wu, H.; Xu, Y.; He, Q.; Ding, L.; Yang, B. The Impact of Lipids on the Cancer-immunity Cycle and Strategies for Modulating Lipid Metabolism to Improve Cancer Immunotherapy. *Acta Pharm. Sin. B* **2023**, *13*, 1488−1497.

(13) Halimi, H.; Farjadian, S. Cholesterol: An Important Actor on the Cancer Immune Scene. *Front. Immunol.* **2022**, *13*, 1057546.

(14) Jiang, Z.; Zhang, G.; Huang, L.; Yuan, Y.; Wu, C.; Li, Y. Transmissible Endoplasmic Reticulum Stress: A Novel Perspective on Tumor Immunity. *Front. Cell Dev. Biol.* **2020**, *8*, 846.

(15) Schwarz, D. S.; Blower, M. D. The Endoplasmic Reticulum: Structure, Function and Response to Cellular Signaling. *Cell. Mol. Life Sci.* **2016**, *73*, 79−94.

(16) Csordás, G.; Weaver, D.; Hajnóczky, G. Endoplasmic Reticulum-Mitochondrial Contactology: Structure and Signaling Functions. *Trends Cell Biol.* **2018**, *28*, 523−540.

(17) Li, Y.; Zhang, X.; Wan, X.; Liu, X.; Pan, W.; Li, N.; Tang, B. Inducing Endoplasmic Reticulum Stress to Expose Immunogens: A DNA Tetrahedron Nanoregulator for Enhanced Immunotherapy. *Adv. Funct. Mater.* **2020**, *30*, 2000532.

(18) Kepp, O.; Menger, L.; Vacchelli, E.; Locher, C.; Adjemian, S.; Yamazaki, T.; Martins, I.; Sukkurwala, A. Q.; Michaud, M.; Senovilla, L.; Galluzzi, L.; Kroemer, G.; Zitvogel, L. Crosstalk between ER Stress and Immunogenic Cell Death. *Cytokine Growth F. R.* **2013**, *24*, 311−318.

(19) Rufo, N.; Garg, A. D.; Agostinis, P. The Unfolded Protein Response in Immunogenic Cell Death and Cancer Immunotherapy. *Trends Cancer* **2017**, *3*, 643−658.

(20) Zhang, L.; Kim, S. B.; Luitel, K.; Shay, J. W. Cholesterol Depletion by TASIN-1 Induces Apoptotic Cell Death through the ER Stress/ROS/JNK Signaling in Colon Cancer Cells. *Mol. Cancer. Ther.* **2018**, *17*, 943−951.

(21) Mandula, J. K.; Chang, S.; Mohamed, E.; Jimenez, R.; Sierra-Mondragon, R. A.; Chang, D. C.; Obermayer, A. N.; Moran-Segura, C. M.; Das, S.; Vazquez-Martinez, J. A.; Prieto, K.; Chen, A.; Smalley, K. S. M.; Czerniecki, B.; Forsyth, P.; Koya, R. C.; Ruffell, B.; Cubillos-

https://doi.org/10.1021/acs.jmedchem.5c02436
J. Med. Chem. 2025, 68, 26328−26347

Ruiz, J. R.; Munn, D. H.; Shaw, T. I.; Conejo-Garcia, J. R.; Rodriguez, P. C. Ablation of the Endoplasmic Reticulum Stress Kinase PERK Induces Paraptosis and Type I Interferon to Promote Anti-tumor T Cell Responses. *Cancer Cell* **2022**, *40*, 1145−1160.
(22) Lu, X.; Qiao, K.; Shaik, F.; Zheng, Y.; Chu, Z.; Qian, H.; Liu, X.; Zhang, W. Evoking Robust Immunogenic Cell Death by Synergistic Sonodynamic Therapy and Glucose Depletion using Au Clusters/Single Atoms Modified TiO2 Nanosheets. *Nano. Res.* **2023**, *16*, 9730−9742.
(23) Estrela, G. R.; Arruda, A. C.; Torquato, H. F. V.; Freitas-Lima, L. C.; Perilhão, M. S.; Wasinski, F.; Budu, A.; Fock, R. A.; Paredes-Gamero, E. J.; Araujo, R. C. Gemfibrozil Induces Anemia, Leukopenia and Reduces Hematopoietic Stem Cells via PPAR-α in Mice. *Int. J. Mol. Sci.* **2020**, *21*, 5050.
(24) Canfora, I.; Pierno, S. Hypertriglyceridemia Therapy: Past, Present and Future Perspectives. *Int. J. Mol. Sci.* **2024**, *25*, 9727.
(25) Huang, J.; Viswakarma, N.; Yu, S.; Jia, Y.; Bai, L.; Vluggens, A.; Cherkaoui-Malki, M.; Khan, M.; Singh, I.; Yang, G.; Rao, M.; Borensztajn, J.; Reddy, J. Progressive Endoplasmic Reticulum Stress Contributes to Hepatocarcinogenesis in Fatty Acyl-CoA Oxidase 1-Deficient Mice. *Am. J. Pathol.* **2011**, *179*, 703−713.
(26) Chan, S.; Sun, R.; Zeng, X.; Choong, Z.; Wang, H.; Watt, M.; Ye, J. Activation of PPARα Ameliorates Hepatic Insulin Resistance and Steatosis in High Fructose-Fed Mice Despite Increased Endoplasmic Reticulum Stress. *Diabetes* **2013**, *62*, 2095−2105.
(27) Shi, B.; Chen, J.; Guo, H.; Shi, X.; Tai, Q.; Chen, G.; Yao, H.; Mi, X.; Zhong, R.; Lu, Y.; Zhao, Y.; Sun, L.; Zhou, D.; Yao, Y.; He, S. ACOX1 Activates Autophagy via the ROS/mTOR Pathway to Suppress Proliferation and Migration of Colorectal Cancer. *Sci. Rep.* **2025**, *15*, 2992.
(28) Chapman, M. J.; Le Goff, W.; Guerin, M.; Kontush, A. Cholesteryl Ester Transfer Protein: at the Heart of the Action of Lipid-modulating Therapy with Statins, Fibrates, Niacin, and Cholesteryl Ester Transfer Protein Inhibitors. *Eur. Heart J.* **2010**, *31*, 149−164.
(29) Staels, B.; Auwerx, J. Role of PPAR in the Pharmacological Regulation of Lipoprotein Metabolism by Fibrates and Thiazolidinediones. *Curr. Pharm. Design* **1997**, *3*, 1−14.
(30) Chowdhury, P. S.; Chamoto, K.; Kumar, A.; Honjo, T. PPAR-Induced Fatty Acid Oxidation in T Cells Increases the Number of Tumor-Reactive CD8+ T Cells and Facilitates Anti-PD-1 Therapy. *Cancer Immunol. Res.* **2018**, *6*, 1375−1387.
(31) (a) Gibson, D. Multi-action Pt(IV) Anticancer Agents; Do we Understand How they Work? *J. Inorg. Biochem.* **2019**, *191*, 77−84. (b) Li, S.; Chen, Y.; Feng, S.; Liu, Z.; Gan, L.; Wang, Q. Autophagy-Targeted Pt(IV) Agents: A New Horizon in Antitumor Drug Development. *Dalton Trans.* **2025**, *54*, 1770−1778.
(32) Wang, Y.; Cai, L.; Li, H.; Chen, H.; Yang, T.; Tan, Y.; Guo, Z.; Wang, X. Overcoming Cancer Resistance to Platinum Drugs by Inhibiting Cholesterol Metabolism. *Angew. Chem., Int. Ed.* **2023**, *62*, No. e202309043.
(33) Sun, P.; Wang, J.; Xie, Q.; Ren, X.; Qiao, X.; Xu, J. Disruption of Lipid Metabolism to Induce Ferroptosis Using Multifunctional Fibrate-Pt(IV) Prodrugs for Cancer Treatment. *Inorg. Chem. Front.* **2024**, *11*, 2914−2931.
(34) Guo, X.; Liang, X.; Liu, J.; Li, Z.; You, Z.; Zhao, D.; Song, Y.; Li, L.; Song, X. Precise Carrier-Free Pt(IV)-Nanobombs for Apoptosis/Ferroptosis Synergistic Tumor Therapy: A new Effective Method to Obtain Good Chemotherapy and Low Toxicity. *J. Med. Chem.* **2025**, *68*, 387−404.
(35) Qiao, X.; Gao, Y.; Zheng, L.; Ding, X.; Xu, L.; Hu, J.; Gao, W.; Xu, J. Targeting ROS-AMPK Pathway by Multiaction Platinum(IV) Prodrugs Containing Hypolipidemic Drug Bezafibrate. *Eur. J. Med. Chem.* **2021**, *223*, No. 113730.
(36) Song, X. Q.; Guo, X.; Ding, Y. X.; Han, Y. X.; You, Z. H.; Song, Y.; Yuan, Y.; Li, L. Gemfibrozil-Platinum(IV) Precursors for New Enhanced-Starvation and Chemotherapy In Vitro and In Vivo. *J. Med. Chem.* **2024**, *67*, 7033−7047.
(37) (a) Zhang, S.; Li, Y.; Liu, S.; Ma, P.; Guo, M.; Zhou, E.; Duan, L.; Fan, J.; Liao, T.; Tan, Q.; Wang, X.; Wu, F.; Jin, Y. Ischemia and Reperfusion Injury Combined with Cisplatin Induces Immunogenic Cell Death in Lung Cancer Cells. *Cell Death Dis* **2022**, *13*, 764. (b) Michaud, M.; Sukkurwala, A. Q.; Sano, F. D.; Zitvogel, L.; Kepp, O.; Kroemer, G. Synthetic Induction of Immunogenic Cell Death by Genetic Stimulation of Endoplasmic Reticulum Stress. *Oncoimmunology* **2014**, *3*, No. e28276.
(38) Feng, P.; Lam, B.; Tseng, S.; Kung, Y.; Farmer, E.; Cheng, M.; Hung, C. NKG2D-Fc Fusion Protein Promotes Antitumor Immunity Through the Depletion of Immunosuppressive Cells. *Cancer Immunol. Immun.* **2020**, *69*, 2147−2155.
(39) Xiong, Z.; Huang, Y.; Cao, S.; Huang, X.; Zhang, H. A New Strategy for the Treatment of Advanced Ovarian Cancer: Utilizing Nanotechnology to Regulate the Tumor Microenvironment. *Front. Immunol.* **2025**, *16*, 1542326.
(40) Miller, D. B.; Spence, J. D. Clinical Pharmacokinetics of Fibric Acid Derivatives (Fibrates). *Clin. Pharmacokinet.* **1998**, *34*, 155−162.
(41) Aputen, A. D.; Elias, M. G.; Gilbert, J.; Sakoff, J. A.; Gordon, C. P.; Scott, K. F.; Aldrich-Wright, J. R. Bioactive Platinum(IV) Complexes Incorporating Halogenated Phenylacetates. *Molecules* **2022**, *27*, 7120.
(42) (a) Song, S.; Shang, X.; Zhao, J.; Hu, X.; Koh, K.; Wang, K.; Chen, H. Sensitive and Selective Determination of Caspase-3 Based on Calixarene Functionalized Reduction of Graphene Oxide Assisted Signal Amplification. *Sensor. Actuat. B-Chem.* **2018**, *267*, 357−365. (b) Debernard, K. A.; Aziz, G.; Gjesvik, A. T.; Paulsen, R. E. Cell Death Induced by Novel Procaspase-3 Activators Can be Reduced by Growth Factors. *Biochem. Bioph. Res. Co.* **2011**, *413*, 364−369.
(43) Wang, J. Q.; Liu, X. M.; Zhu, Z. S.; Li, Z.; Xie, C. Z.; Qiao, X.; Feng, Y. K.; Xu, J. Y. Fluoxetine-Conjugated Platinum(IV) Prodrugs Targeting eEF2K and Conquering Multidrug Resistance against Triple-Negative Breast Cancer. *J. Med. Chem.* **2025**, *68*, 9661−9680.
(44) Liang, G.; Sadhukhan, T.; Banerjee, S.; Tang, D.; Zhang, H.; Cui, M.; Montesdeoca, N.; Karges, J.; Xiao, H. Reduction of Platinum(IV) Prodrug Hemoglobin Nanoparticles with Deeply Penetrating Ultrasound Radiation for Tumor-Targeted Therapeutically Enhanced Anticancer Therapy. *Angew. Chem., Int. Ed.* **2023**, *62*, No. e202301074.
(45) (a) Bélanger, F.; Fortier, E.; Dubé, M.; Lemay, J.; Buisson, R.; Masson, J.; Elsherbiny, A.; Costantino, S.; Carmona, E.; Mes-Masson, A.; Wurtele, H.; Drobetsky, E. Replication Protein A Availability during DNA Replication Stress Is a Major Determinant of Cisplatin Resistance in Ovarian Cancer Cells. *Cancer Res.* **2018**, *78*, 5561−5573. (b) Yuan, X.; Zhang, W.; He, Y.; Yuan, J.; Song, D.; Chen, H.; Qin, W.; Qian, X.; Yu, H.; Guo, Z. Proteomic Analysis of Cisplatin- and Oxaliplatin-induced Phosphorylation in Proteins Bound to Pt-DNA Adducts. *Metallomics* **2020**, *12*, 1834−1840.
(46) (a) Zhang, C.; Xu, C.; Gao, X.; Yao, Q. Platinum-based Drugs for Cancer Therapy and Anti-tumor Strategies. *Theranostics* **2022**, *12*, 2115. (b) Wang, M.; Li, G.; Jiang, G.; Cai, J.; Zhong, W.; Huang, R.; Liu, Z.; Huang, X.; Wang, H. Dual-Targeting Tumor Cells Hybrids Derived from Pt(IV) Species and NF-κB Inhibitors Enables Cancer Therapy through Mitochondrial Dysfunction and ER Stress and Overcomes Cisplatin Resistance. *Eur. J. Med. Chem.* **2024**, *266*, No. 116095.
(47) (a) Wei, T.; Chen, L.; Shi, P.; Wang, C.; Peng, Y.; Yang, J.; Liao, X.; Yang, B.; Gao, C. Platinum(IV) Drugs with Cannabidiol Inducing Mitochondrial Dysfunction and Synergistically Enhancing Anti-Tumor Effects. *J. Inorg. Biochem.* **2024**, *254*, 112515. (b) Canta, A.; Pozzi, E.; Carozzi, V. A. Mitochondrial Dysfunction in Chemotherapy-Induced Peripheral Neuropathy (CIPN). *Toxics* **2015**, *3*, 198−223.
(48) Zhou, Y.; Li, M.; Wang, Z.; Lin, X.; Xu, Y.; Feng, S.; Miao, J. AMPK/Drp1 Pathway Mediates Streptococcus Uberis-induced Mitochondrial Dysfunction. *Int. Immunopharmacol.* **2022**, *113*, No. 109413.
(49) (a) Biswas, A.; Kashyap, P.; Datta, S.; Sengupta, T.; Sinha, B. Cholesterol Depletion by MβCD Enhances Cell Membrane Tension

and Its Variations-Reducing Integrity. *Biophys. J.* **2019**, *116*, 1456−1468. (b) Kerkhofs, M.; Bittremieux, M.; Morciano, G.; Giorgi, C.; Pinton, P.; Parys, J. B.; Bultynck, G. Emerging Molecular Mechanisms in Chemotherapy: Ca2+ Signaling at the Mitochondria-associated Endoplasmic Reticulum Membranes. *Cell Death Dis* **2018**, *9*, 334. (c) Nakamura, H.; Takada, K. Reactive Oxygen Species in Cancer: Current Findings and Future Directions. *Cancer Sci.* **2021**, *112*, 3945−3952.

(50) (a) Van Meer, G.; Voelker, D. R.; Feigenson, G. M. Membrane Lipids: Where They Are and How They Behave. *Nat. Rev. Mol. Cell Biol.* **2008**, *9*, 112−124. (b) Wang, W.; Agellon, L. B.; Michalak, M. Endoplasmic Reticulum Calcium Dictates the Distribution of Intracellular Unesterified Cholesterol. *Cell Calcium* **2018**, *76*, 116−121.

(51) Li, J.; Zi, X.; Fang, J.; Liang, M.; Ju, M.; Sun, Z.; Shen, B.; Zhang, X. Endoplasmic Reticulum Stress Induces Liquid-Liquid Phase Separation of GRP78 and Modulates Protein Aggregation Dynamics. *Acs Sensors* **2025**, *10*, 4535−4543.

(52) Elfiky, A. A.; Baghdady, A. M.; Ali, S. A.; Ahmed, M. I. GRP78 Targeting: Hitting Two Birds with A Stone. *Life Sci.* **2020**, *260*, No. 118317.

(53) Ren, J. L.; Chen, Y.; Zhang, L. S.; Zhang, Y. R.; Liu, S. M.; Yu, Y. R.; Jia, M. Z.; Tang, C. S.; Qi, Y. F.; Lu, W. W. Intermedin1−53 Attenuates Atherosclerotic Plaque Vulnerability by Inhibiting CHOP-mediated Apoptosis and Inflammasome in Macrophages. *Cell Death Dis.* **2021**, *12*, 436.

(54) Zhu, M.; Wang, T.; Wang, H.; Wang, H.; Chen, H.; Zhang, S.; Guo, Y.; Li, H.; Hui, H. LW-213 Induces Immunogenic Tumor Cell Death via ER Stress Mediated by Lysosomal TRPML1. *Cancer Lett.* **2023**, *577*, No. 216435.

(55) Bekeschus, S. ROS-targeting of Melanoma Cells Provides Immuno-Protection Against Tumor Growth. *Free Radical Bio. Med.* **2018**, *128*, S62.

(56) Ding, D.; Jiang, X. Advances in Immunogenic Cell Death for Cancer Immunotherapy. *Small Methods.* **2023**, *7*, No. e2300354.

(57) Talman, V.; Kivelä, R. Cardiomyocyte-Endothelial Cell Interactions in Cardiac Remodeling and Regeneration. *Front. Cardiovasc. Med.* **2018**, *5*, 101.

(58) Ma, X.; Bi, E.; Lu, Y.; Su, P.; Huang, C.; Liu, L.; Wang, Q.; Yang, M.; Kalady, M. F.; Qian, J.; Zhang, A.; Gupte, A. A.; Hamilton, D. J.; Zheng, C.; Yi, Q. Cholesterol Induces CD8+ T Cell Exhaustion in the Tumor Microenvironment. *Cell Metab.* **2019**, *30*, 143−156.

(59) Huang, Q.; Wu, X.; Wang, Z.; Chen, X.; Wang, L.; Lu, Y.; Xiong, D.; Liu, Q.; Tian, Y.; Lin, H.; Guo, J.; Wen, S.; Dong, W.; Yang, X.; Yuan, Y.; Yue, Z.; Lei, S.; Wu, Q.; Ran, L.; Xie, L.; Wang, Y.; Gao, L.; Tian, Q.; Zhou, X.; Sun, B.; Xu, L.; Tang, Z.; Ye, L. The Primordial Differentiation of Tumor-Specific Memory CD8+ T Cells as Bona Fide Responders to PD-1/PD-L1 Blockade in Draining Lymph Nodes. *Cell* **2022**, *185*, 4049−4066.

(60) Wang, Q.; Cao, Y.; Shen, L.; Xiao, T.; Cao, R.; Wei, S.; Tang, M.; Du, L.; Wu, H.; Wu, B.; Yu, Y.; Wang, S.; Wen, M.; OuYang, B. Regulation of PD-L1 through Direct Binding of Cholesterol to CRAC Motifs. *Sci. Adv.* **2022**, *8*, No. eabq4722.

(61) Overacre-Delgoffe, A. E.; Chikina, M.; Dadey, R. E.; Yano, H.; Brunazzi, E. A.; Shayan, G.; Horne, W.; Moskovitz, J. M.; Kolls, J. K.; Sander, C.; Shuai, Y.; Normolle, D. P.; Kirkwood, J. M.; Ferris, R. L.; Delgoffe, G. M.; Bruno, T. C.; Workman, C. J.; Vignali, D. A. A. Interferon-γ Drives Treg Fragility to Promote Anti-tumor Immunity. *Cell* **2017**, *169*, 1130−1141.

(62) Hebbar Subramanyam, S.; Turyne Hriczko, J.; Schulz, S.; Look, T.; Goodarzi, T.; Clarner, T.; Scheld, M.; Kipp, M.; Verjans, E.; Böll, S.; Neullens, C.; Costa, I.; Li, Z.; Gan, L.; Denecke, B.; Schippers, A.; Floess, S.; Huehn, J.; Schmitt, E.; Bopp, T.; Wasmuth, H.; Winograd, R.; Beyaert, R.; Lambrecht, B.; Zenke, M.; Wagner, N.; Ohl, K.; Tenbrock, K. CREB Regulates Foxp3+ST-2+ TREGS with Enhanced IL-10 Production. *Front. Immunol.* **2025**, *16*, 1601008.

(63) Overacre-Delgoffe, A. E.; Vignali, D. A. A. Treg Fragility: A Prerequisite for Effective Antitumor Immunity? *Cancer Immunol. Res.* **2018**, *6*, 882−887.

(64) (a) Calls, A.; Torres-Espin, A.; Tormo, M.; Martínez-Escardó, L.; Bonet, N.; Casals, F.; Navarro, X.; Yuste, V. J.; Udina, E.; Bruna, J. A Transient Inflammatory Response Contributes to Oxaliplatin Eurotoxicity in Mice. *Ann. Clin. Transl. Neur* **2022**, *9*, 1985−1998. (b) Authier, N.; Balayssac, D.; Marchand, F.; Ling, B.; Zangarelli, A.; Descoeur, J.; Coudore, F.; Bourinet, E.; Eschalier, A. Animal Models of Chemotherapy-evoked Painful Peripheral Neuropathies. *Neurotherapeutics* **2009**, *6*, 620−629.

(65) Hans, G.; Deseure, K.; Vercauteren, M. Altered Sensitivity to Mechanical Stimulation during Prolonged Subcutaneous Administration of Endothelin-1 in Rats. *J. Pain Res.* **2009**, *2*, 67−73.

(66) Kobayashi, M.; Watanabe, K.; Yokoyama, S.; Matsumoto, C.; Hirata, M.; Tominari, T.; Inada, M.; Miyaura, C. Capsaicin, a TRPV1 Ligand, Suppresses Bone Resorption by Inhibiting the Prostaglandin E Production of Osteoblasts, and Attenuates the Inflammatory Bone Loss Induced by Lipopolysaccharide. *Int. Sch. Res. Not.* **2012**, *2012*, 1.

(67) Wang, W.; He, X.; Wang, X.; Zhao, T.; Muraoka, O.; Tanabe, G.; Xie, W.; Zhou, T.; Xing, L.; Jin, Q.; Jiang, H. Glutathione-depleted Cyclodextrin Pseudo-polyrotaxane Nanoparticles for Anti-inflammatory Oxaliplatin(IV) Prodrug Delivery and Enhanced Colorectal Cancer Therapy. *Chin. Chem. Lett.* **2024**, *35*, No. 108656.

(68) Lee, J. Y.; Choi, H. Y.; Park, C. S.; Jang, C.; Lee, K. T.; Lee, J. Y.; Youn, I.; Yune, T. Y. Inhibition of COX-2 Alleviates Lumbar Spinal Stenosis-induced Chronic Mechanical Allodynia in Rats. *Int. Immunopharmacol.* **2019**, *75*, No. 105738.

https://doi.org/10.1021/acs.jmedchem.5c02436
J. Med. Chem. 2025, 68, 26328−26347